HHS Public Access

Author manuscript

Cell. Author manuscript; available in PMC 2023 September 01.

Published in final edited form as:

Cell. 2022 September 01; 185(18): 3356–3374.e22. doi:10.1016/j.cell.2022.07.025.

Sublethal Cytochrome-c release generates drug-tolerant persister cells

Halime Kalkavan[1], **Mark J. Chen**[1], **Jeremy C. Crawford**[1], **Giovanni Quarato**[1], **Patrick Fitzgerald**[1], **Stephen W.G. Tait**[2,3], **Colin R. Goding**[4], **Douglas R. Green**[1,5,*]

[1]Department of Immunology, St. Jude Children's Research Hospital, Memphis, TN 38105, USA

[2]Cancer Research UK Beatson Institute, Switchback Road, Glasgow G61 1BD, UK

[3]Institute of Cancer Sciences, University of Glasgow, Switchback Road, Glasgow G61 1BD, UK

[4]Ludwig Institute for Cancer Research, Nuffield Department of Clinical Medicine, University of Oxford, Headington, Oxford OX37DQ, United Kingdom

[5]Lead contact

SUMMARY:

Drug-tolerant persister cells (persisters) evade apoptosis upon targeted and conventional cancer therapies and represent a major non-genetic barrier to effective cancer treatment. Here we show that cells that survive treatment with pro-apoptotic BH3 mimetics display a persister phenotype that includes colonization and metastasis *in vivo* and increased sensitivity towards ferroptosis by GPX4 inhibition. We found that sublethal mitochondrial outer membrane permeabilization (MOMP) and Holocytochrome c release are key requirements for the generation of the persister phenotype. The generation of persisters is independent of apoptosome formation and caspase activation, but instead, cytosolic Cytochrome c induces activation of Heme-regulated Inhibitor (HRI) kinase and engagement of the integrated stress response (ISR) with consequent synthesis of ATF4, all of which are required for the persister phenotype. Our results reveal that sublethal Cytochrome c release couples sublethal MOMP to caspase-independent initiation of an ATF4-dependent, drug-tolerant persister phenotype.

[*]Correspondence: douglas.green@stjude.org.

AUTHOR CONTRIBUTIONS

H.K. and D.R.G. designed the experiments. H.K. performed and analyzed the experiments. M.C. and J.C.C. performed bioinformatic analyses. G.Q., P.F., C.G., S.T. provided resources, performed and analyzed specific experiments. H.K. and D.R.G. wrote the manuscript.

DECLARATION OF INTERESTS

The authors declare no competing interests. D.R.G. consults for Ventus Therapeutics, Inzen Therapeutics, and Horizon Therapeutics.

STATISTICAL ANALYSIS

Please refer to the legend of the figures for description of sample sizes and statistical tests performed. Data were plotted and analyzed with GraphPad Prism 9.0 software. Differences were considered statistically significant when the p-value was less than 0.05, and otherwise not significant (ns).

Further information and requests for resources and reagents should be directed to and will be fulfilled by the Lead Contact, Douglas Green (douglas.green@stjude.org).

Graphical Abstract

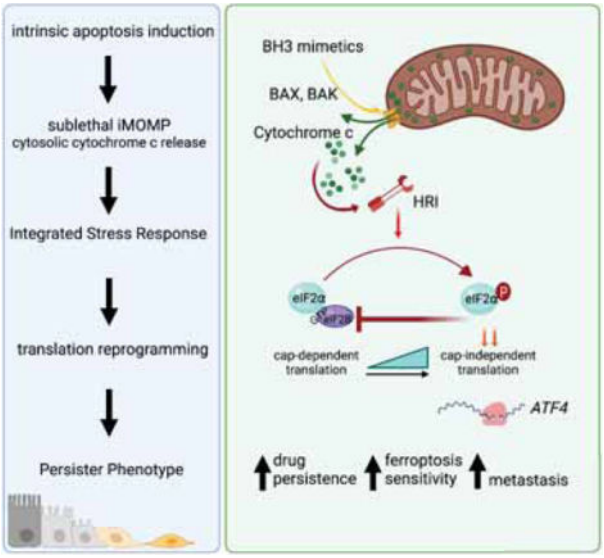

Abstract

Cancer cells that survive treatment with pro-apoptotic BH3 mimetics do so by undergoing sub-lethal mitochondrial outer membrane permeabilization and induction of a stress response via cytochrome c but independent of caspases. They thus acquire a persister state that enables metastatic colonization in vivo.

Keywords

Mitochondrial permeabilization; BCL-2 family; BH3 mimetics; drug-persistence; persister phenotype; cancer; Cytochrome c; ATF4; HRI; EMT; metastasis; drug-resistance; GPX4; ferroptosis; lung adenocarcinoma

INTRODUCTION

In addition to genetic events that mediate resistance to anti-cancer therapies, a major contribution to cancer relapse is the emergence of drug-tolerant cells, a phenomenon called persistence. A key feature of such persister cells is that, in contrast to resistant cells, their drug-unresponsive phenotype is acquired and provides a temporary survival-advantage towards treatment.

Persister cells (PS) can be functionally defined as cells that remain alive following a cell death-inducing treatment, without the selection for resistance mutations. PS from different cancer cell lines treated under different conditions often have a number of features in common that differ from the untreated, parental cells (PT) (Shen et al., 2020). These features, which can serve as a “PS phenotype” include a) transient tolerance of the initial treatment and often other toxic treatments, b) an acquired dependence on the lipid peroxidase, GPX4, c) reduced cell cycle kinetics, and d) similar gene expression profiles, often including, an epithelial to mesenchymal transition (EMT) signature. The ability to

adapt to microenvironmental stresses by altering phenotype is often evolutionary conserved and is related to survival strategies in the face of starvation or diapause (García-Jiménez and Goding, 2019; Rehman et al., 2021). Although the features of therapy-tolerant persister cells have been defined, the key molecular events that enable a cancer cell to bypass cell death on exposure to pro-apoptotic cancer therapeutics, especially after initial engagement of the apoptotic machinery, remain poorly understood.

As the best studied and most complex form of regulated cell death, apoptosis can be triggered by a wide range of cellular stresses (e.g. oncogenic, metabolic, genetic) and therapeutics that converge on the intrinsic pathway of apoptosis (Singh et al., 2019). Central to this pathway is the mitochondrion, which harbors in its intermembrane space (IMS) crucial caspase activators such as Holocytochrome c (Kalkavan and Green, 2018).

The BCL-2 family effector proteins BAX, BAK and BOK are responsible for mitochondrial outer membrane permeabilization (MOMP), triggering apoptosis (Bhola and Letai, 2016). Anti-apoptotic proteins bind and hinder effector protein function. The pro-apoptotic BH3-only proteins bind via their BH3 domains to anti-apoptotic proteins and/or directly to BAX and BAK to engage MOMP (Garrido et al., 2006; Tait and Green, 2013). This important function of the BH3 domain has been exploited therapeutically as BH3 mimetics, such as Navitoclax, Venetoclax, and MCL-1 inhibitors (Kalkavan and Green, 2018; Merino et al., 2018).

The initiation of the apoptotic cascade does not inevitably lead to cell death. Ongoing studies have focused on the consequences of incomplete MOMP (iMOMP) and sublethal caspase activity on cell fate, challenging the binary character of MOMP to reveal that cells do not always commit to cell death (Tait et al., 2010). Instead, iMOMP can occur, resulting in a more nuanced caspase activation and cell survival (Ichim and Tait, 2016).

A key and rapid adaptive survival response to a wide range of triggers relies on the phosphorylation of the translation initiation factor eIF2α by one of four kinases, EIF2AK1/HRI, EIF2AK2/PKR, EIF2AK3/PERK and EIF2AK4/GCN2, each responsive to distinct upstream stresses (Pakos-Zebrucka et al., 2016). The resulting translational reprogramming suppresses global cap-dependent translation and enables translation of a subset of mRNAs encoding proteins that function to alleviate the stress and promote survival (Tian et al., 2021). Among these is Activating Transcription Factor 4 (ATF4) that initiates a gene expression program that in the short-term promotes survival by increasing nutrient uptake and autophagy, and suppressing oxidative stress (Costa-Mattioli and Walter, 2020).

Here we reveal that following treatment with pro-apoptotic BH3 mimetics, drug-tolerant persisters arise as a consequence of the activation of mitochondrial-nuclear communication relayed by iMOMP and Cytochrome c-dependent activation of HRI, leading to ATF4 synthesis and function. We found that the persister phenotype, induced by treatment with BH3 mimetics, is dependent on MOMP and the release of Cytochrome c, as well as HRI and ATF4. Further, we define a BAX, BAK, BOK-dependent, ATF4-dependent PS gene signature that can be found in lung cancer patients with residual disease following therapy.

RESULTS

BH3 mimetics induce persister cancer cells

Cancer treatments generally converge on intrinsic apoptosis as their main cell death effector mechanism (Singh et al., 2019). We utilized the highly specific BH3 mimetics ABT-737 and S63845 (S6) (Kotschy et al., 2016), which target BCL-2, BCL-XL, BCL-w (ABT-737) and MCL1 (S6). We first confirmed maximal on-target doses by comparing wildtype (WT) to *BAX* and *BAK* double knock-out (DKO) or *BAX, BAK* and *BOK* triple knock-out (TKO) cells (Figures 1A, S1A and S1B). WT therapy-persisting cells (persister cells, PS) were released from therapy for 1 day and upon re-exposure to the drugs, proved to be less sensitive to treatment with BH3 mimetics (Figures 1B and S1C). However, a longer drug holiday of 6d restored the drug-sensitivity of the initially drug-tolerant persisters to parental (PT) sensitivity (Figures 1B and S1C), suggesting that the drug-tolerant persister state was transient. We then examined the behavior of PT and BH3 mimetic-induced PS *in vivo*. We generated PC9 PS by treatment with BH3 mimetics and compared the ability of PS to colonize the lungs to that of the untreated PT cells. PC9 cells were transduced with mNeonGreen or mCherry, and were then used to generate PT and PS, respectively, allowing us to distinguish between each population *in vivo*. Equal numbers of mNeonGreen-expressing PT and mCherry-expressing PS cells were simultaneously injected i.v. into the tail veins of immunocompromised NSG mice. Nine weeks after injection, lungs were primarily colonized by PS and not by PT (Figure 1C). Similarly, intra-vital assessment of luciferase-labeled cells after tail vein injection showed that mice injected with BH3 mimetic-induced PS from the colon cancer cell line HCT116 had significantly higher tumor burden when compared to mice injected with HCT116 PT cells (Figure 1D and 1E).

Since these colonization assays mimic only the late phase of the metastatic cascade after intravasation, we exploited an *in vivo* orthotopic lung tumor model where we simultaneously injected PC9 PS and PT labelled with either Cell Trace Violet (CTV) or carboxyfluorescein succinimidyl ester (CFSE), respectively, into the left lungs of recipient animals. An advantage of these dyes is the strong and equal labeling of cells (Figure 1F). In line with previous studies *in vitro*, our PS displayed a slower proliferative rate than PT on day 2 after orthotopic injection (Figure 1F) (Chen et al., 2012; Oren et al., 2021; Shen et al., 2020). To test the invasiveness and intravasation ability of the implanted lung tumor cells, we measured circulating-tumor cells (CTC) in blood collected from the right heart ventricle. Interestingly, we found significantly more circulating PS than PT at day 2 (Figure 1G). Next, we measured the metastatic ratio of the injected cells, which we defined as the cancer cell percentage in the contralateral lung divided by its percentage in the primary-injection site. In line with the CTC result, the metastatic ratio revealed a higher metastatic capacity of PS generated from PC9 or A549 cells (Figure 1G and S1D).

Next, we tested whether PS generated using BH3 mimetics led to cross-resistance towards other cancer therapies. We compared PT and PS derived from PC9 and HT29 cells and treated them with targeted and conventional standard-of-care cancer therapies in vitro (Figures 1H and S1E). In both models, PS exhibited significantly increased viability after exposure to each drug.

Recent discoveries on drug-tolerant persisters revealed acquired dependency on the lipid hydroperoxidase GPX4 for their survival (Hangauer et al., 2017; Yang et al., 2016). Viability analysis of our apoptosis PS showed increased sensitivity to GPX4-inhibition by RSL3 compared to PT in PC9 and HT29 cells (Figures 1I, S1F and S1G). In line with this finding, the membrane-targeted lipid ROS sensor C11-BODIPY (Yang et al., 2014) revealed increased lipid ROS levels (Figure S1H). Moreover, the expression of ChaC Glutathione-Specific Gamma-Glutamylcyclotransferase 1 (CHAC1) was upregulated, while the Glutamate-Cysteine Ligase Catalytic Subunit (GCLC) was downregulated in PS when compared to their PT counterpart (Figure S1I), both indicative of decreased glutathione metabolism that may explain the increased dependence on GPX4 (Tang et al., 2021).

To identify common characteristics of PS generated with diverse therapies, we performed RNAseq on therapy-persisting PC9 cells obtained by treatment with conventional chemotherapy, targeted therapy, or BH3 mimetics (Figure 1J). Our analysis revealed common gene expression signatures related to metastasis and invasion, cellular stress responses, upregulated inflammatory signaling and EMT, and downregulated fatty acid metabolism, oxidative phosphorylation and mTORC1 signaling (Figures 1J and S1J). Collectively, these data indicate that PS generated using BH3 mimetics have the gene expression and phenotypic characteristics of drug-tolerant persister cells generated under different conditions as described by others.

The persister phenotype depends largely on Bcl-2 effectors

By binding to the BH3-groove, BH3 mimetics enable the dissociation of the effector proteins BAX and BAK from the antiapoptotic proteins and cause MOMP. However, antiapoptotic, proapoptotic and effector BCL-2 proteins are involved in diverse cell functions, and the BH3 domain is also necessary for the interaction between BH3-only proteins and anti-apoptotic proteins (Kale et al., 2018; Popgeorgiev et al., 2018). To determine whether the presence of BCL-2 family effector proteins is necessary for our persister phenotype we tested PC9 cells deficient in *BAX, BAK*, and *BOK* (TKO). We treated these TKO cells with our BH3 mimetics and compared them to the PT cells. Lung colonization capacity of PS (Figure 2A) and their metastatic potential (Figure 2B) were dependent on the BCL2 effector proteins. Moreover, the sensitivity to RSL3-induced ferroptosis was similar between untreated and BH3 mimetic-pretreated TKO cells (Figure 2C and S2A). In line with this finding, C11-BODIPY staining as well as *CHAC1* and *GCLC* transcripts were not changed in BH3 mimetic-pretreated TKO cells when compared to PT (Figures S2B and S2C).

To elucidate the downstream pathways that might be involved in the engagement of the persister phenotype, we conducted RNAseq of WT and TKO cells treated with control (MOCK) or BH3 mimetics. Enrichment analysis of BAX, BAK, BOK-dependent, differentially expressed genes (DEGs) in PS versus PT (Figure 2D) further confirmed the overall dependence on BCL-2 effector proteins for our previously identified pathways, such as the upregulation of NFκB signaling, EMT and the downregulation of mTORC1 signaling and fatty acid metabolism, and revealed additional pathways such as interleukin signaling and “response to EIF2AK1 (HRI) to heme deficiency” (Figures 2E and 2F). Interestingly,

many of the DEGs identified have been associated with metastasis, angiogenesis, and cancer immune evasion (Figure 2G and S2D). Moreover, a stratification of the top 10 up- and down regulated DEGs into pathways such as EMT and the cell cycle further identified potential genes implicated in our persister phenotype (Figure 2H).

Previous work has shown that downregulation of glutathione metabolism correlates with sensitivity towards ferroptosis (Oren et al., 2021). Indeed, our data reveals several downregulated DEGs that participate in the glutathione metabolism pathway in WT PS but not in TKO that have been treated with BH3 mimetics (Figure 2I).

Transcriptomic trajectories reveal a transient ISR expression profile in BH3 mimetic persisters

To gain more insight into the mechanisms that underlie the generation of the persister phenotype, we performed single-cell RNAseq on PC9 PT and corresponding PS 1, 3, and 7 days (PS1D, PS3D, and PS7D respectively) after BH3 mimetic treatment. Uniform manifold approximation and projection (UMAP) analysis revealed the distinct transcriptomes of PT and the initial (PS1D) persister phenotype, as well as the trending of late PS (PS3D, PS7D) towards PT (Figure 3A). To dissect the initial events that distinguish PS from PT and late PS, we next performed a trajectory analysis also known as pseudotime, which is a computational method that organizes a population of cells into a progression consistent with patterns of identified, dynamic processes, presumed to represent changes in the cell states over time (Berge et al., 2020; Street et al., 2018). Whereas late PS exhibited comparable pseudotime states to PT, PS1D were enriched for a clearly distinct and earlier state, suggestive of a gradual return to the PT phenotype after BH3 mimetic treatment (Figures 3A). Interestingly, genes from clusters activated relatively early in pseudotime were significantly enriched for the EMT pathway (cluster 1) and the integrated stress response (ISR; cluster 3; Figures 3B, 3C, S2E and S2F). In contrast, clusters corresponding to later pseudotimes (2 and 4) were enriched for genes central to DNA replication and cell cycle progression, both hallmarks for late PS and PT. These cluster enrichments also corresponded to differences in gene set module scores across the PT and PS conditions in real time, independently linking these biological processes with the experimental conditions (Figure 3D). These data also help to indicate specific genes that may underly the PS phenotype with broad involvement in metabolism, inflammation, and cell cycle (Figure S2F). Furthermore, the upregulation of genes involved in the ISR in 1 day PS that gradually waned over the ensuing days corresponded to the transient state of PS (Figures 3D and S2F).

BH3 mimetics induce a BCL-2 effector-dependent ISR, independent of caspase activation

We explored if and how the ISR was related to MOMP and the persister phenotype. Consistent with our transcriptomic analysis, we confirmed engagement of the ISR upon BH3 mimetic treatment by detection of the phosphorylation of eIF2α observed within the first hour after treatment and subsequent detection of ATF4 (Figure 4A). Consequently, PS contained elevated levels of nuclear ATF4 compared to PT as assessed by confocal imaging (Figure 4B, 4C and 4D).

To determine if the translation switch occurs in our BH3 mimetic-induced PS, we engineered an ATF4 translation reporter (Figure 4E). Treatment with BH3 mimetics led to increased reporter activity in WT cells (Figures 4F and S3A). This was inhibited by 2BAct, which prevents phosphorylated eIF2α from reprogramming protein translation (Hetz et al., 2019), and by the ISR inhibitor ISRIB (Figure S3B) (Rabouw et al., 2019). Significantly, BH3 mimetic-treated *BAX, BAK, BOK* TKO cells failed to activate the luciferase reporter (Figure 4F).

Incomplete MOMP, followed by minimal caspase activity upon apoptosis failure can be associated with cancer cell aggressiveness, mutability, and metastasis (Berthenet et al., 2020; Ichim and Tait, 2016; Oberst et al., 2016). To test whether caspase activation is also necessary for ATF4 activation, we treated Casp9-deficient cells with BH3 mimetics. These cells are unable to activate the caspase cascade (Kuida et al., 1998), but retained the ability to induce the luciferase translation reporter upon BH3 mimetic treatment (Figure 4G). Concordantly, APAF1- and Casp*9*-deficient cells expressed ATF4 in response to treatment with BH3 mimetics (Figure 4H), as did cells treated with the pan-Caspase inhibitor Q-VD-OPh (Caserta et al., 2003) (Figure 4I).

We then tested which eIF2α kinase is responsible for eIF2α phosphorylation and ATF4 translation. Upon treatment, only cells silenced for HRI (EIF2AK1) displayed decreased luciferase reporter activity compared to cells silenced for the other kinases (Figure 4J). Similarly, treatment with BH3 mimetics of WT but not HRI-deficient cells led to increased nuclear ATF4 protein (Figures 4K and S3C). Therefore, BH3 mimetics induce an ISR via HRI, which is dependent on the BCL-2 effectors but independent of caspase activation.

Engagement of sublethal MOMP is crucial for ISR activation

The dependency on BAX and BAK for the generation of PS suggested that iMOMP in surviving cells might be essential for ISR engagement. We engineered a reporter to reveal mitochondrial permeabilization, using a split-superfoldGFP (sfGFP) system (Figures 5A and B) in which GFP1–10 was fused to mCherry and was localized with a fused IMS-localized tail sequence, while a double GFP11 beta strand was localized to the cytoplasm. We predicted that MOMP would enable the translocation of GFP11 into the IMS by passive diffusion, where it could then associate with GFP1–10 to fluoresce green (Figure 5B). Using this MOMP sensor in A549 PS cells revealed an increased GFP signal (Figure 5C), which was prevented by silencing of *BAX* and *BAK* (Figure 5D and S3D). In contrast, cells treated with Raptinal, which induces MOMP in a BAX, BAK, BOK-independent manner (Heimer et al., 2019), showed an increased signal in both siNT and si*BAX*, si*BAK* treated cells (Figure 5D). We next tested if the activation of ATF4 protein expression was associated with the extent of MOMP in our PS. Indeed, GFP-high cells that had undergone more extensive sublethal MOMP than GFP-low PS showed higher ATF4 (Figure 5E). Moreover, GFP-high PS displayed increased metastatic potential compared to their GFP-low PS counterparts (Figure 5F). These results support the idea that BCL-2 effector proteins promote ATF4 expression and increased colonization by PS *in vivo* due to their role in MOMP. Accordingly, WT cells displayed eIF2α phosphorylation and ATF4 expression upon BH3 mimetics or Raptinal treatment (Figure 5G), while *BAX, BAK, BOK* TKO cells

only did so upon treatment with Raptinal (Figures 4F and 5H). Further, Raptinal-treated TKO cells showed an increased metastatic potential *in vivo* (Figure S3E), which was not observed when such cells were treated with BH3 mimetics (Figure 2B).

To test the possibility that MOMP, independent of apoptosome and caspase activation, could drive metastatic potential in PS, we also generated PS from APAF1- and Caspase-9-deficient PC9 cells. Indeed, intra-pulmonal injection of PT and PS cells from both lines showed increased metastatic ratio in PS compared to the PT counterpart (Figures 5I and J).

Cytochrome C activates HRI and engages the persister phenotype

Cytochrome c (encoded by *CYCS*) has a crucial role in the activation of APAF1 and caspases following MOMP (Hao et al., 2005; Li et al., 2000). Strikingly, silencing of *CYCS* significantly reduced ATF4 activation upon BH3 mimetic treatment (Figures 6A, S4A to C). Additionally, when bovine Cytochrome c was added to cytosolic extracts of WT cells, it led not only to caspase activation as previously described (Liu et al., 1996) but also eIF2α phosphorylation, which depended on the presence of HRI (Figure 6B, 6C and S4D).

Next, we asked if the Cytochrome c K72R mutant, which is incapable of activating APAF1 (Hao et al., 2005), can engage the ISR upon treatment with BH3 mimetics (Figures S4E, S4F and S4G). Treatment of cells expressing either WT and or mutant Cytochrome c led to an increase of ATF4, whereas Cytochrome c-deficient cells harboring only an empty vector control (pEVEC) showed no ATF4 protein expression upon treatment (Figure 6D). Similarly, A549 cells that express $CYCS^{K72R}$, upon silencing of endogenous *CYCS* with an UTR-targeting siRNA, expressed ATF4 upon treatment with BH3 mimetics, while silencing of both endogenous and ectopically expressed mutant Cytochrome c significantly diminished ATF4 expression (Figure S4H and I). Silencing of Holocytochrome c Synthase (*HCCS*), required for the generation of mature Cytochrome c, also prevented the synthesis of ATF4 upon BH3 mimetic treatment (Figures 6E and S4C).

We then generated PS from Cytochrome c-deficient cells reconstituted, or not, with WT or K72R mutant Cytochrome c. While BH3 mimetic-pretreated or untreated *CYCS*-deficient cells showed similar sensitivity towards a variety of drugs tested, PS from either reconstituted cell lines displayed drug-tolerance (Figures 6F, 6G, S5A and B). Additionally, in comparison to PT, PS from cells with reconstituted mutant Cytochrome c displayed enhanced metastatic potential (Figure 6H). While we observed no difference in recovery of BH3 mimetic-pretreated or untreated *CYCS*-deficient cells, it is likely that such cells do not survive *in vivo*, and therefore we did not examine their metastatic potential. Therefore, the ability of BH3 mimetics to generate PS is dependent upon Cytochrome c but independent of its ability to induce apoptosis.

We then asked if the genes that had been identified as regulated in PS in a BAX, BAK-dependent manner were also regulated in a *CYCS*-dependent manner. Genes that are relevant for glutathione metabolism, and hence might account for the RSL3 sensitivity of PS, were up- or downregulated by treatment with BH3 mimetics, dependent upon *CYCS* expression (Figure 6I). Interestingly, the expression of CHAC1, which is involved in glutathione (GSH) degradation (Crawford et al., 2015), was upregulated only in the presence

of Cytochrome c. In contrast, the CHAC cation transport regulator homolog 2 (CHAC2) which competes with CHAC1 to prevent GSH degradation (Wang et al., 2017), was downregulated in a Cytochrome c-dependent manner. Similarly, genes including CREB5, ATF3, PDK1 and PTGS2 showed significantly diminished expression in *CYCS*-deficient BH3 mimetic treated cells compared to *CYCS* reconstituted PS (Figure 6J and S5C).

We then performed experiments with recombinant eIF2α and HRI and purified bovine Cytochrome c. We observed increased phosphorylation of eIF2α upon addition of Cytochrome c (Figures 6K and S5D). HRI is constitutively active, and is inhibited by hemin (Berlanga et al., 1998; Igarashi et al., 2008; Yang et al., 1992). We found that the inhibition of HRI by hemin did not occur in the presence of Cytochrome c (Figure 6L). To further investigate if Cytochrome c and HRI physically interact in cells upon treatment with BH3 mimetics, we performed immunoprecipitation of endogenous Cytochrome c and IgG control from PC9 APAF1-deficient cells that had been treated with or without BH3 mimetics, resulting in co-immunoprecipitation of HRI and Cytochrome c (Figure 6M) (A low-level of co-immunoprecipitation of HRI with Cytochrome c in untreated cells was likely due to release of Cytochrome c upon lysis). In another approach, we expressed HRI-mClover or mClover in A549 cells before BH3 mimetic treatment (Figure S5E). Immunoprecipitation of HRI-mClover resulted not only in the co-immunoprecipitation of Cytochrome c, but also of endogenous HRI, indicative of an activation-induced dimerization of HRI, which has been described by others (Bauer et al., 2001). Finally, we generated lysates from HRI-mClover- or mClover-expressing A549 cells and incubated them with equine Cytochrome c. Immunoprecipitation of HRI-mClover resulted not only in the pull-down of Cytochrome c, but also of eIF2α, the substrate of HRI (Figure S5F). Therefore, the engagement of HRI and the ISR, leading to the PS phenotype, is a direct effect of the release of Cytochrome c to the cytosol and its interaction with HRI following iMOMP.

A Cytochrome c – HRI - ATF4 pathway drives the phenotype of persistence

The involvement of ATF4 in various aspects of cancer aggressiveness has been described (Dey et al., 2015). In line with this, cells silenced for ATF4 and treated with BH3 mimetics revealed that the statistically significant upregulation of the EMT pathway is dependent on ATF4 (Figure 7A). Several well-defined transcriptional targets of ATF4 showed increased expression at early pseudotime, characteristic of PS1D in our scRNAseq analysis (Figure S6A). We therefore asked whether ATF4 is the main driver of our observed persister phenotype. Since BH3 mimetic-induced PS also showed an upregulation of other stress-associated modulators, such as NRF2 and HO-1, both of which have been associated with cancer aggressiveness (Bialk et al., 2018; Fox et al., 2020; Inguaggiato et al., 2001; Niture and Jaiswal, 2012), we tested the response to BH3 mimetics upon silencing these regulators. The absence of ATF4 led to significant therapy sensitivity and reduced the occurrence of PS in different cell lines (Figures 7B and S6B to D), while NRF-2 and HO-1 appeared to be dispensable. Early PS displayed an increased sensitivity towards 2BAct (Figure 7C). To test the role of ATF4 in the persister phenotype, we generated ATF4-deficient cells (Figure S6E) and treated them with BH3 mimetics. Surviving cells were exposed to a variety of pro-apoptotic anti-cancer drugs, revealing equal or higher sensitivity to the same drugs as *ATF4*$^{-/-}$ PT (Figure 7D).

Since BH3 mimetics induce BCL-2 effector-mediated apoptotic cell death, we wondered if the effector proteins were present in PS. BAX but not the other effector proteins were decreased in PS (Figure S6F). It has been reported that the absence of BAX can lead to chemoresistance (Erler et al., 2004; Haefen et al., 2004). Silencing of *BAX*, *BAK* or *BOK* in PC9 cells before treatment with BH3 mimetics revealed that the absence of *BAX* alone almost completely abolished sensitivity to the drugs (Figure 7E and S6G) and also decreased sensitivity towards other therapies in PC9 cells (Figure S6H). To evaluate if the decrease in BAX relied on the Cytochrome c-dependent activation of the ISR, we tested *CYCS*-, *ATF4*- and *HRI*-deficient cells treated with BH3 mimetics (Figure 7F and 7G). We observed that BAX was decreased only in WT cells that had survived BH3 mimetic treatment. Transcript levels of *BAX* were similar in Cytochrome c proficient and deficient cells (Figure S6I), suggesting that post-transcriptional regulation was responsible for the decreased BAX levels in our PS. One possible explanation for the reduction in BAX might be the engagement of autophagy, which can target BAX for degradation (Feng et al., 2018; Guan et al., 2015). ATF4 has been shown to induce autophagy (B'chir et al., 2013; Rzymski et al., 2009) and consistent with this, we observed that the degradation of p62/SQSTM1, a consequence of autophagy, occurred in BH3 mimetic-treated WT but not *ATF4*- or *HRI*-deficient cells (Figure 7G).

We examined the sensitivity to GPX4 inhibition and found that the increased sensitivity in PS was abrogated in ATF4- and HRI-deficient BH3 mimetic survivors (Figures 7H, 7I, S6J and S6K), which corresponded to changes in lipid-peroxidation (Figure S6L) and *CHAC1* and *GCLC* expression (Figures S6M and S6N). Next, we tested the metastatic capacity of ATF4- and HRI-deficient cells and their BH3 mimetic treatment-surviving cells *in vivo*. The increased metastatic ratio of WT PS cells (Figure 1G) was largely abolished in the absence of ATF4 (Figure 7J) or HRI (Figure 7K).

To determine whether ATF4 activation could induce a persister phenotype independent of iMOMP, we treated cells with Tunicamycin (TN), which leads to ATF4 translation independent of BCL-2 effector proteins or Caspase-9 (Figure S6Q). These TN-induced PS revealed decreased sensitivity towards diverse chemotherapies (Figure S6R) and increased sensitivity towards GPX4 inhibition with RSL3 (Figure S6S).

Finally, we performed a stringent comparative analysis of differentially expressed genes in BH3 mimetic-treated WT cells that are absent in treated *ATF4*- or *BAX* and *BAK*-silenced cells (Figure 7L), which revealed several target genes implicated in inflammatory signaling and immune evasion, metabolism, migration and invasion (Figure 7M). We suggest that this gene set represents an "apoptosis persister signature." To test its clinical relevance, we applied gene set enrichment analysis on published scRNAseq data from lung adenocarcinoma samples (Maynard et al., 2020). Strikingly, gene set module scores for up- or down-regulated apoptosis persister genes were significantly greater among samples from patients with residual disease (RD) compared to those with treatment-naïve (TN) or progressive disease (Figure 7N). Further, the Reactome HRI gene set score was increased in RD, while the KEGG glutathione metabolism gene score was significantly decreased in RD compared to TN (Figure 7O).

Because our experimental results identified HRI as the relevant kinase for translation reprogramming and generation of the persister phenotype in PC9 lung adenocarcinoma (LUAD) cells, we wondered if HRI expression was present in cancer samples. Pathology samples from lung, breast, gastric and ovary cancer showed much stronger expression of HRI compared to their normal tissue counterparts (Figure S7A). *HRI* gene expression is significantly higher in various tumors when compared to the normal tissues (Figures S7B and C), including LUAD and colon adenocarcinomas. Since RNAseq data revealed a high inter-patient variation in *HRI* expression (Figure S7C), we asked if *HRI* (*EIF2AK1*) expression correlates with patient survival. We interrogated disease free survival and overall survival of patients with *HRI* high (1st quartile) versus low (4th quartile) tumors. Many HRI-high tumor-bearing patients showed decreased survival and significantly increased hazard ratios compared to patients with HRI-low tumors (Figures 7P and S7D, S7E, S7F and S7G).

DISCUSSION

Our work uncovers a new function for Cytochrome c in promoting survival in the presence of a sublethal incident. We provide evidence of how iMOMP and the release of Cytochrome c drives translation reprogramming in cells that survive the initiation of apoptosis. As a major consequence of eIF2α phosphorylation, *ATF4* mRNA translation leads to the initiation of the various downstream pathways that are critical for the persister phenotype, including metabolic reprogramming, cell cycle inhibition, immune evasion, and EMT induction.

Additionally, we found that our persister phenotype includes an increased metastatic potential of PS. While the often-described EMT signature of persister cells is suggestive of an increased metastatic capacity (Nieto, 2011; Shen et al., 2020) and sensitivity towards ferroptosis correlates with both EMT and increased metastasis (Hangauer et al., 2017; Ubellacker et al., 2020; Viswanathan et al., 2017; Yang et al., 2014), a direct connection between a persister phenotype and metastasis has to the best of our knowledge not been previously described.

We identified the heme-regulated inhibitor (HRI) as the critical kinase that leads to eIF2α phosphorylation and translational reprogramming in PC9 cells treated with BH3 mimetic drugs. Our fundamental knowledge about HRI originated in research on erythropoiesis, where iron deficiency leads to the autophosphorylation and dimerization of HRI and thus its activation (Berlanga et al., 1998; Miksanova et al., 2006; Rafie-Kolpin et al., 2003; Yang et al., 1992; Zhang et al., 2019). This evolutionarily conserved pathway appears to be present in non-hematopoetic cells, including cancer cells where we found that high expression of HRI correlates with decreased survival of cancer patients. Our work reveals the crucial impact of HRI on cancer cell survival by linking sublethal Cytochrome c release to HRI activation. It also provides a possible explanation for the increased sensitivity towards ferroptosis in drug-tolerant persisters when GSH metabolism is altered, as a linked trade-off for survival when translational reprogramming takes place. Transcriptomic changes in the metabolome including a downregulation of the mTORC1 pathway that is dependent on sublethal apoptosis initiation and ATF4 activation is in line

with findings where mitochondrial dysfunction was accompanied by HRI activation and mTORC1 downregulation (Condon et al., 2021; Zhang et al., 2019).

MOMP can play a role in caspase-independent cell death (CICD), where death is relayed by a loss of mitochondrial function (Lartigue et al., 2009). Previous work on CICD indicated that in the absence of caspase activation cells that had evaded death after the engagement of MOMP and Cytochrome c release were dependent on the activation of the autophagy machinery and intact mitochondria (Colell et al., 2007). Since ATF4 is a well-known activator of autophagy (Sui et al., 2013), our results provide a possible mechanistic explanation for how pro-apoptotic effectors can promote survival. We do not know, however, whether engagement of autophagy is indeed responsible for the transient drug tolerance we observe in PS, or if this applies to PS generated under other conditions.

Previous work has also documented how mitochondrial dysfunction can lead to the cytosolic accumulation of mitochondrial proteins and a mitochondrial unfolded protein response (UPR^{mt}), which in turn activates the expression of ATF4 (Melber and Haynes, 2018). In contrast, our results indicate that unlike the UPR^{mt}, the engagement of ATF4 by the ISR in persister cells does not primarily rely on mitochondrial damage itself but instead is dependent on Cytochrome c release to the cytosol. Recent evidence revealed that release of the IMS protein DELE1 after cleavage by OMA1 can activate the ISR via HRI (Fessler et al., 2020; Guo et al., 2020). However, whether MOMP is necessary for DELE1 release and the biological consequences of DELE1 release in our system remain unclear.

Additionally, iMOMP can lead to sublethal caspase activation (Liu et al., 2015; Miles and Hawkins, 2017; Oberst et al., 2016; Paoli et al., 2013). Although, our data supports a mechanism that is independent of caspases, there is evidence that caspase activation in a drug-persisting cancer cell induces EMT, can activate PKR and increases mutability by the sublethal activation of caspase-activated DNAse (CAD) (Berthenet et al., 2020; Miles and Hawkins, 2017; Saelens et al., 2001). Taken together, it is possible that adaptive responses can be engaged on various levels after sublethal MOMP initiation.

Limitations of the study

Our approach in this study was to investigate – without any other perturbations – the role of sublethal engagement of apoptosis. Thus, we created controlled circumstances to induce PS by the use of BH3 mimetics and *in vitro* induction of cell death, followed by assessment of the persister phenotype *in vitro* and *in vivo*. The extent to which our findings apply to PS induced by other drug treatments and the further application of our findings to patient data from human primary cancers and residual disease will be important. Since other therapeutic treatments can likely engage the ISR via other mechanisms than Cytochrome c-induced HRI activity, the generalizability of our BH3 mimetic persister cells and the mechanism we uncovered requires further investigation. This especially applies to *in vivo* settings where cells that survive therapeutic insult are more challenging to study.

STAR+METHODS

RESOURCE AVAILABILITY

Lead contact—Further information and requests for resources and reagents should be directed to and will be fulfilled by the lead contact, Douglas R Green (Douglas.Green@stjude.org).

Materials availability—Plasmids generated in this study are obtainable upon request.

Data and code availability—Single-cell RNA-seq data have been deposited at GEO (accession: GSE189639) and are publicly available as of the date of publication. Accession numbers are listed in the key resources table. Original western blot images and microscopy data reported in this paper will be shared by the lead contact upon request.

All original code has been deposited at GitHub (https://github.com/markgene/MC015_Persister_public) and is publicly available as of the date of publication. DOIs are listed in the key resources table.

Any additional information required to reanalyze the data reported in this paper is available from the lead contact upon request.

METHODS

EXPERIMENTAL MODEL AND SUBJECT DETAILS

Mice: RAG1 k.o. (Figure 1E) and NOD.Cg-Prkdcsscid Il2rgtm1Wjl/SzJ (NSG) (all other animal models) mice were used for tumormodels. Age and sex matched cohorts of 5 to 12 weeks old females and males were used in all experiments. The St. Jude Institutional Animal Care and Use Committee approved all procedures in accordance with the Guide for the Care and Use of Animals. All mice were housed in pathogen-free facilities, in a 12-hour light/dark cycle in ventilated cages, with chow and water supply *ad libitum*.

Cells: Human lung cancer cell line PC9 was purchased from Millipore Sigma (Cat# 90071810). Human lung cancer cell line A549 was kindly provided by Richard J. Webby (St. Jude Children's Research Hospital). Human colorectal carcinoma cell line HCT116 was a gift from Richard Youle (Wang and Youle, 2011). Cancer cell line HT29 (human colorectal) and H226 (human Mesothelioma) were purchased from ATCC.

Cells were maintained in complete DMEM media (10% fetal bovine serum (FBS), 2 mM L-glutamine and 100 units/ml penicillin-streptomycin). For culturing *CYCS* k.o. cells medium was additionally supplemented with 50μg/ml uridine (Sigma) and 1 mM sodium pyruvate (GIBCO). All cells used in this study were cultivated at 37°C with 5% CO_2.

All the cell lines used in tumor studies were confirmed as mycoplasma negative using MycoAlert Mycoplasma Detection kit (Lonza #LT07). All cell lines have been authenticated by Hartwell Center (St. Jude Children's Research Hospital).

Clonogenic survival was assessed by methylene blue staining.

METHOD DETAILS

In vivo colonization and FACS analysis—PC9 stably expressing mNeon Green were used as PT. PC9 cells stably expressing mCherry were treated with ABT737 1.5 μM and S63845 3 μM for 6 h followed by wash and release into complete medium for 2 h, to generate PS. EasySep Dead Cell Removal (Annexin V) kit (Stemcell Technologies) was used to harvest live cells according to the manufacturer's protocol. PT and PS were injected in combination (0.4×10^6 cells in total per mouse) into the teil vein of NSG mice (200μl in DMEM). When animals were getting symptomatic due to disease progression they have been euthanized in accordance with our existing humane endpoints (9 weeks post injection) to assess organ colonization. For ex vivo processing of lung colonization lungs of animals were resected and kept in PBS. Tissue was minced using scissors and digested in trypsin supplemented with 100 μg/ml Liberase TM (Sigma-Aldrich) and 200 μg/ml Deoxyribonuclease I (Sigma-Aldrich) for 30 min incubation at 37°C 5% CO_2. Organs were then resuspended in DMEM containing 5% FCS, pipetted up-and down and passed through a 40 μM strainer. Cells were then washed in FACS Buffer (1g/l sodium azide, 10 g/l PBS powder, 2.5mM EDTA, 1% FCS in MilliQ filtered water). Fixation was performed using 2% formalin in PBS for 10 minutes at room temperature. Cells were washed twice in permeabilization buffer (1mg/ml Saponin in FACS buffer). Cells were then stained with Chromotek GFP- and RFP booster for 30 minutes at 4°C. A final wash in permeabilization buffer was performed before FACS analysis.

In vivo colonization and IVIS Bioluminescence Imaging—PC9 WT or BAX, BAK, BOK TKO cells stably expressing tdTomato and firefly luciferase were used as PT. Another batch of the same cells were treated with ABT737 1.5 μM and S63845 3 μM for 6 h followed by wash and release into complete medium for 2 h, to generate PS. EasySep Dead Cell Removal (Annexin V) kit (Stemcell Technologies) was used to harvest live cells according to the manufacturer's protocol. PT and PS were injected into separate (0.4×10^6cells per mouse) into the teil vein of NSG mice (200μl in DMEM). Optical imaging of Bioluminescence and/or Fluorescence was performed by using IVIS Spectrum or IVIS-200 imaging systems. 5–10 minutes prior to imaging, animals were injected i.p. with D-Luciferin (15 mg/ml in sterile saline) at a dose of 150 mg/kg (10 μL/g of body weight). After administration, animals were anesthetized using Isoflurane (1.5–2% delivered in 100% O2 at 1 l/min) and maintained via nosecone on heated imaging bed within the system for the duration of the scan. Following imaging, animals were allowed to recover on a heating blanket under observation and supplemented with oxygen as required.

Orthotopic lung tumors (conventional, non-surgical approach) and FACS analysis—Cells were treated with ABT737/S63845 (PC9 1.5/3 μM, A549 5/10 μM) 4–6h followed by wash and release into complete medium for 2 h, to generate PS. EasySep Dead Cell Removal (Annexin V) kit (Stemcell Technologies) was used to harvest live cells according to the manufacturer's protocol. PT were stained with CFSE and PS with CTV label retention dye (Thermo Scienfic) according to the manufacturer's protocol, washed twice in complete medium before further processing. Single injection tumor cell suspensions with combinations of PT and PS in Matrigel were prepared in one-milliliter syringes with 30-gauge hypodermic needles for an injection volume of 50 μl (2×10^6 total cells

per mouse). Mice were anesthetized with isoflurane and placed in right lateral decubitus position. Local disinfection of the left posterior thorax was performed. Transdermal intrapulmonal injections have been performed at the posterior medial line juxta below the inferior angle of the scapula, through the intercostal space, 5–7 mm into the thorax. After injection mice were turned to the left lateral decubitus position and observed for approximately 15 min. Note: This non-surgical approach is comparable to the published surgical procedure for intrapulmonary injection (Isobe et al., 2013; Okimoto et al., 2017).

For ex vivo processing of lungs to assess metastatic ratio, left (primary injection site) and right (metastatic side) lungs of animals were resected and kept separately in PBS. Tissue was minced using scissors and digested in trypsin supplemented with 100 μg/ml Liberase TM (Sigma-Aldrich) and 200 μg/ml Deoxyribonuclease I (Sigma-Aldrich) for 30 min incubation at 37°C 5% CO_2. Organs were then resuspended in DMEM containing 5% FCS, pipetted up-and down and passed through a 40μM strainer.

Cells were stained for surface markers CD45-APC (in initial experiments also CD31-PECy7) for 20 minutes at 4°C. Erythrocyte lysis (NH_4Cl_2 150mM, $KHCO_3$ 10mM, EDTA 0.1mM, pH7.2) was performed at room temperature for 2 minutes. Cells were then washed in FACS Buffer (1g/l sodium azide, 10 g/l PBS powder, 2.5mM EDTA, 1% FCS in MilliQ filtered water) before FACS analysis.

For analysis of circulating tumor cells (CTC) 300 μl blood was collected from the right heart ventricle after mice had been euthanized and collected into vessels containing 30 μl of EDTA (Invitrogen). 100 μl of blood sample per mouse was stained for surface marker CD45-APC for 20 minutes at 4°C. Erythrocyte lysis (NH_4Cl_2 150mM, $KHCO_3$ 10mM, EDTA 0.1mM, pH7.2) was performed at room temperature for 2 minutes. Cells were then washed in FACS Buffer (1g/l sodium azide, 10 g/l PBS powder, 2.5mM EDTA, 1% FCS in MilliQ filtered water) before FACS analysis.

Transient transfection: DNA and siRNA transient transfection was performed over 48 h using Viafect™ (Promega) for HEK, A549 and HT29, FugeneHD® (Promega) for PC9, A549 and HCT116 or Lipofectamine™ 3000 (Invitrogen) for any cell line, and Lipofectamine™ RNAiMAX transfection reagents, respectively. Cells were transfected at 50–75% confluence in serum-free Opti-MEM (Invitrogen) as per the manufacturers' instructions. The siRNA oligos used were either purchased from Dharmacon as ON-TARGETplus siRNA pools of 4 oligos or from IDT as single siRNAs (see Supplementary Table 4).

Generation of Cell lines—For stable transfections, cells were transfected with a modified Piggybac expression system (Magnúsdóttir et al., 2013) for continuous expression. To remove the inducible expression promoter, we replaced the preexisting 6× Tet-Operators with a CMV promoter and placed the gene of interest under its control. Additionally, another variant of this backbone has been established by replacement of the puromycin resistance gene with zeocin or blasticidin resistance. Stable transfections were then performed by transfection of cells with the expression vector pPB together with a vector expressing the PiggyBac transposase which integrates the expression cassette. Stable transductants

were selected after adding 200 μg/mL zeocin™ (Invitrogen), 0.2 μg/mL puromycin (Sigma-Aldrich) or 20 μg/mL blasticidin (Invitrogen) with replacement of the medium every 2 days for max. 14 days or were sorted by flow cytometry for Cerulean-, Venus-, GFP-, or mCherry-positive cells.

Generation of knock out cells was performed by usage of the CRISPR-Cas9 technology. The different lentiviral vectors used are either carrying Cas9 sequence and sgRNA sequence (CRISPRv2 GFP, Addgene, a gift from David Feldser; Px458 pSpCas9(BB)-2A-GFP, Addgene, a gift from Feng Zhang, pSpCas9(BB)-2A-mCherry) or sgRNA carrying vectors (pLKO5.sgRNA.EFS.PAC, Addgene a gift from Benjamin Ebert) were transfected simultaneously with Cas9 expressing vectors mentioned above (Heckl et al., 2014; Ran et al., 2013; Walter et al., 2017). The primer sequences for sgRNAs are listed in Supplementary Table S3 (Lopez et al., 2016; Shalem et al., 2014). Transiently transfected cells were selected after 0.2 μg/mL puromycin (Sigma-Aldrich) or 20 μg/mL blasticidin (Invitrogen) with replacement of the medium every 2 days for max. 10 days or were sorted by flow cytometry for GFP-, or mCherry-positive cells. Single clones were selected and expanded to generate *BAX, BAK, BOK* triple knock-out cells and *CYCS*-deficient cells.

Flow Cytometry: For intracellular staining cells were fixed and permeabilized according to the manufacturer's instructions using Intracellular Fixation & Permeabilization Buffer Set (BD). To monitor Cytochrome c release, cells were incubated with 20μg/ml digitonin in PBS (Sigma-Aldrich) for 10 minutes on ice before fixation and further staining procedure. For nuclear staining of ATF4, the Foxp3 Fixation/Permeabilization (eBioscience) was used according to the manufacturer's protocol.

Measurement of cellular lipid peroxidation was performed using BODIPY 581/591 C11 (Thermo Fisher). PT and PS have been treated in 12-well plates with 2μM RSL3 overnight in the presence or absence of 40 μM Deferoxamine mesylate salt (DFO). Cells were collected in Hank's Balanced Salt Solution (HBSS; Gibco) and incubated with 2 μM BODIPY 581/591 C11 for 20 min at 37 °C. Cells were then washed twice in HBSS and analyzed via FACS.

Data acquirement and analysis was performed in a spectral analyzer (CYTEK Aurora 5-laser and 3-Laser) and data was processed using FlowJo software (Tree Star).

IncuCyte Analysis: Cell-death kinetics were monitored by the IncuCyte S3 imaging system (Essen Bioscience). Dead cells were stained with 400 ng/ml propidium iodide (PI) or 25 nM SYTOX Green (Invitrogen). SYTOX Green- or PI-positive cells were quantified by the IncuCyte image analysis software (Essen Bioscience). Data were expressed as positive events per well. Error bars represent the SD from the mean for triplicate samples.

Cytosolic extracts: Cell-free (cytosolic) extracts were generated as previously described (Liu et al., 1996). In our studies we followed the detailed protocol that is provided by the Cold Spring Harbor Protocols (McStay and Green, 2014). Ten 15cm dishes of confluent cells, were washed with ice-cold PBS. Cells were then scraped and harvested into 50ml conical tubes filled with ice-cold PBS. After centrifugation (at 250g for 5min. at 4°C), the

supernatant has been removed and the pellet volume has been estimated. An equal volume of homogenization buffer (10mM HEPES pH7, 5mM $MgCl_2$, 0.67 mM DTT, 1 protease inhibitor cocktail tablet (Roche)) has been used to completely resuspend the cells with a 1ml pipette tip. After an incubation of 15 min on ice, the cell suspension has been passed 10 times through a 22-gauge needle using a 3ml syringe. Testing aliquots of the lysate, this procedure has been repeated until more than 80% of nuclei stained blue in Trypan blue solution. Then, the homogenized cell suspension has been centrifuged at 15,000g for 30min 4°C in a 1.5ml microcentrifuge tube, the supernatant has been transferred to a new tube, and the same centrifugation step has been repeated. Next, the supernatant has again been transferred to a new tube and centrifuged at 100,000g for 1h 4°C. Finally, the supernatant has been passed through a 0.22μm centrifugal filter. Protein concentration has been determined by measuring absorbance at 280nm.

HRI eIF2α kinase assay: For kinetic analyses of eIF2α phosphorylation, HRI (25 nM) with or without 100nM Cytochrome c was incubated in kinase buffer (20 mM Tris buffer pH 7.4, 40 mM KCl, 3 mM magnesium acetate and 1 mM DTT) at room temperature for 15 min. A titration of 0.05–12 μg eIF2α was prepared in assay buffer and supplemented with 50 μM ATP. The reaction was initiated by adding the substrate mix to the enzyme mix and then incubated at room temperature for 5 min (initial velocity conditions). The HRI kinase reaction rate using 25 nM HRI is linear for the first 20 min (Figure S5C) as previously published (Guo et al., 2020). The amount of reaction product (phosphorylated eIF2α) formed during the first 5 min was used as the initial velocity. Kinetic constants were determined using least-squares fit with Prism v.9.

qRT-PCR: mRNA for qRT-PCR were extracted using the RNeasy Mini Kit (Qiagen). Reverse transcription reactions were performed with M-MLV reverse transcriptase (Invitrogen) following the manufacturer's protocol and using random hexamers (IDT). The primer sequences for qPCR are listed in Supplementary Table S5 (Kim et al., 2010; Spandidos et al., 2008, 2010; Wang et al., 2012). Real-time PCR was performed with SYBR™ Green using the QuantStudio™ 7 Flex Real-Time PCR System (Applied Biosystems).

Western blotting: Cells were either lysed in cell lysis buffer (50mM Tris-Cl pH 7.4, 150 mM NaCl, cOmplete® protease inhibitors cocktail (Roche), and 0.5% Nonidet P-40) or directly in sample buffer (BioRad) containing DTT. To detect phosphorylation, the cell lysis buffer was supplemented with phosSTOP® phosphatase inhibitor cocktail (Roche).

Immunoprecipitation: A549 cells were transiently transfected with HRI-mClover or mClover constructs. 24 h after transfection cells were treated with ABT737 1.5μM, S6 3μM and QvD 20μM for 4 h, washed in ice-cold PBS, trypsinized and again washed in PBS, followed by an incubation in 2% PFA/PBS for 15 minutes at room temperature, turning end-to-end. Then samples were quenched in ice-cold glycine/PBS (0.7M) for 5 minutes at room temperature again turning end-to-end and afterwards washed twice in ice-cold PBS. Immunoprecipitation was performed using GFP-Trap_MA beads (Chromotek, gtma20) according to the manufacturer's instructions. Lysis was performed in 10mM Tris/Cl pH

7.5, 80mM NaCl, 0.5% NP40 substitute, Phosphatase-inhibitor (Roche) and EDTA-free Protease-inhibitor cocktail (Millipore Sigma). Lysate supernatants were incubated with beads at 4°C for 4h. Proteins captured on the magnetic beads were boiled in 2× SDS loading dye for 10 min before subjecting to SDS–PAGE and western blotting.

For in vitro incubation of HRI-mClover or mClover expressing A549 lysates with equine Cytochrome c, A549 cells were transiently transfected with constructs for 24h, washed in ice-cold PBS, trypsinized and again washed before lysis (same buffer as above). After lysis, supernatants were incubated with 100nm of equine Cytochrome c for 20 minutes at room temperature, followed by GFP-Trap_MA bead incubation at 4°C for 4h. IP was performed as described above.

For Co-immunoprecipitation of endogenous proteins, PC9 *APAF1*$^{-/-}$ cells were treated with ABT737 1.5 μM and S6 3 μM for 3.5h, then washed in ice-cold PBS, trypsinized and again washed. This was followed by an incubation in 2% PFA/PBS for 15 minutes at room temperature, turning end-to-end. Then samples were quenched in ice-cold glycine/PBS (0.7M) for 5 minutes at room temperature again turning end-to-end and afterwards washed twice in ice-cold PBS. Lysis was performed in 10mM Tris/Cl pH 7.5, 80mM NaCl, 0.5% NP40 substitute, Phosphatase-inhibitor (Roche) and EDTA-free Protease-inhibitor cocktail (Millipore Sigma). Lysate supernatants were incubated with either anti-Cytochrome c antibody (BD #556432, 20 μg) or normal mouse IgG (sc-2025, 20 μg) at 4°C overnight, followed by 2h incubation with Protein A/G PLUS-Agarose (sc-2003, Santa Cruz) at 4°C, and complexes were washed 5 times in cell lysis buffer. Proteins captured were eluted by boiling in 2× SDS loading dye for 10 min before subjecting to SDS–PAGE and western blotting.

Single cell RNA seq: PC9 cells were treated with ABT737 1.5 μM and S63845 3 μM for 6h and then washed and released in complete culture medium overnight (PS1D), 3 days (PS3D) or a week (PS7D) to obtain PS. EasySep Dead Cell Removal (Annexin V) kit (Stemcell Technologies) was used to harvest live cells from PT, PS1D, PS3D and PS7D according to the manufacturer's protocol. The single cell suspension was resuspended in phosphate-buffered saline containing at the concentration of 1200 cell/ μl. A total of 20000 cells were loaded into each well of a Chromium single cell capture chip (Chromium Single Cell A Chip Kit, 10X Genomics). The captured single cells on droplets were processed for cell lysis, reverse transcription followed by library amplification (Chromium Single Cell 3' Library and gel Bead Kit v2, 10X Genomics) and indexing as per the manufactures protocol.

RNAseq: For comparison of different treatments of PC9 cells total RNA was extracted from PT or PS which were generated by treatment with ABT737 1.5 μM and S63845 3 μM for 6 h, or Erlotinib 5 μM for 3 d or Paclitaxel 0.5 μM for 3 d (n=3/group).

RNA quality was assessed by 2100 Bioanalyzer RNA 6000 Nano assay (Agilent). Libraries were prepared using TruSeq Stranded mRNA kits (Illumina) and subjected to 100 cycle paired-end sequencing on the Illumina HiSeq platform.

scRNA-seq data processing: The libraries were sequenced on Illumina HiSeq with 500 million clusters per library. Cell Ranger (10X Genomics) (version 6.0.1) was used to process the raw sequencing data and align the reads to the GRCh38 reference genome. The count matrix was filtered as follows. All mitochondrial and ribosomal protein genes were removed, as were any genes expressed in 0.15% cells or less per library. Genes expressed at high level similar to mitochondrial and ribosomal genes were also removed, including MALAT1, FTL and FTH1. Cells were removed by individual libraries based on the number of genes per cell, proportion of reads mapped to mitochondrial and ribosomal genes (see supplementary table S2 for the threshold). Each library was normalized by dividing the UMI counts of each gene within a cell by the total number of UMIs in the cell and natural-log transformed using log1p function in R base package. A cell cycle score of each cell was calculated using CellCycleScoring function in Seurat package (Stuart et al., 2019) and cell cycle genes (Tirosh et al., 2016). The libraries were down-sampled to the same number of cells (3753 cells), merged and scaled by number of genes, proportion of reads mapped to mitochondrial genes, and cell cycle phases S and G2M scores. Principal component analysis (PCA) was run on the scaled data. The cells were projected onto a 2-dimension space of Uniform Manifold Approximation and Projection (UMAP) using the first 40 principal components of PCA as input and the parameters a=200, b=0.4 (other parameters were defaulted).

Trajectory analysis and differential expression along the pseudotime: Trajectory analysis was performed with Slingshot using UMAP projection as input, starting cells of PS1D sample, and approx_points=150 (Street et al., 2018). The analysis of gene expression along the trajectory was performed with tradeSeq R package followed its official documentation with default parameters (Berge et al., 2020); 299 genes were differentially expressed along the pseudotime testing against 2-fold change (l2fc=1) identified using associationTest function. The genes were clustered using hierarchical clustering method with the modelled gene expression (centered and scaled) and cut into 4 clusters.

Gene set score calculation: The gene set score measures the average gene expression level of given a gene set. It was calculated using AddModuleScore function of Seurat package with default parameters. The gene sets were defined based on bulk RNA-seq in this study (Figure 7N) or from MSigDB database (Liberzon et al., 2015) (Figure 7O).

Bulk RNA-seq data analysis: Paired-end sequencing reads were mapped by the pipeline of St Jude Center for Applied Bioinformatics. Basically, the reads were trimmed with Trim Galore (version 0.5.0) (Krueger et al., 2021) with default parameters. Then reads were aligned to the reference mouse hg38 assembly plus ERCC spike-in sequences using STAR (version 2.7.5a) (Dobin and Gingeras, 2015). The resulting alignments, recorded in BAM file, were sorted, indexed, and marked for duplicates with Picard MarkDuplicates function (version 2.19.0) (Broad-Institute, 2019). Transcript quantification was calculated using RSEM (Li and Dewey, 2011). To examine if there is a global change in gene expression, RUVg function in RUVSeq package was used for normalization followed by DESeq2 with reads mapped ERCC spike-in according to RUVSeq manual (Risso et al., 2014). No global change was found, and differential gene expression analysis was carried

out using DESeq2 with standard procedure (normalized by the median-of-ratios method with default parameters (Love et al., 2014).

Enrichment analysis: Gene set enrichment analysis (GSEA) was performed against MSigDB database (Liberzon et al., 2015) with R package clusterProfiler (version 3.18.1) (Yu et al., 2012) (Figure 1J, 7A, S1J). Wald statistic calculated from DESeq2 was used for gene ranking. Over-representation enrichment was performed against MSigDB with R package clusterProfiler (version 3.18.1) (Figures 2E, 2F, S2F).

Gene expression and survival analysis: For HRI gene expression comparison between human normal and cancer samples we utilized RNA sequencing expression data of 9,736 tumors and 8,587 normal samples from the TCGA and the GTEx projects which were analyzed by the Webtool GEPIA2 (Tang et al., 2019). Same datasets and software were used to determine disease free survival and overall survival in dependence of HRI expression in various tumors estimated by Mantel-Cox test (Figure S7D, S7E).

Gene expression, survival and clinical information of TCGA LUAD cohort were downloaded from UCSC Xena (Goldman et al., 2020). EGFR-mutated lung adenocarcinomas were filter by sample_type of “Primary tumor” and egfr_mutation_performed of “YES”. Gene expression RNAseq (IlluminaHiSeq) was used, in which the expression value is log2(x+1) where x is the RSEM value. Survival analysis was performed in R (Figure 7P).

Kaplan Meier Plots have been generated by use of the online webtool Kaplan-Meier Plotter with univariate Cox regression analysis. Patients have been trichotomized into 1st and 4th quartile for *HRI* (217735_s_at) expression using the GSE51105 dataset for gastric cancer (Brasacchio et al., 2018; Busuttil et al., 2014; Szász et al., 2016), GSE3149 dataset for ovarian cancer (Bild et al., 2006; Győrffy et al., 2012) and TCGA dataset for renal papillary cell cancer (Nagy et al., 2021) (Figure S7F) and E-MTAB-365 dataset for breast cancer relapse-free survival (Figure S7G) (Guedj et al., 2012; Győrffy, 2021; Rème et al., 2013).

Pathology: The antibody used for immunohistochemistry corresponding to human normal and cancer tissue was polyclonal rabbit anti-HRI HPA016496 (Millipore Sigma). Images were obtained from the Human Protein Atlas (https://www.proteinatlas.org/ENSG00000086232-EIF2AK1).

Supplementary Material

Refer to Web version on PubMed Central for supplementary material.

ACKNOWLEDGEMENTS

The authors thank Richard Cross and Greig Lennon (SJCRH) for technical assistance and Aseem Ansari, Paul Thomas, Cliff Guy, Gustavo Palacios, Shelbi Christgen, Diego Rodriguez, Joelle Magne, Emilio Boada Romero (SJCRH), Jane-Jane Chen (MIT), and Cristina Muñoz Pinedo (Idibell, Barcelona) for thoughtful insights and discussions. We also thank the Hartwell Center for RNA sequencing and the Center for In Vivo Imaging and Therapeutics (supported by SJCRH, NCI R50 CA211481, and NCI P30 CA021765) for preclinical imaging (SJCRH). This work was supported by ALSAC (SJCRH), and by the U.S. National Cancer Institute grant R35 CA231620 to D.R.G. and the German Research Foundation (DFG, KA 4830/1-1) to H.K.

Original Piggybac vectors were provided by Kazuhiro Murakami (RIKEN, Kobe, Japan). As indicated, some of the results published here are based upon data generated by the TCGA Research Network: https://www.cancer.gov/tcga.

REFERENCES

Bauer BN, Rafie-Kolpin M, Lu L, Han A, and Chen J-J (2001). Multiple Autophosphorylation Is Essential for the Formation of the Active and Stable Homodimer of Heme-Regulated eIF2α Kinase †. Biochemistry-Us 40, 11543–11551. 10.1021/bi010983s.

B'chir W, Maurin A-C, Carraro V, Averous J, Jousse C, Muranishi Y, Parry L, Stepien G, Fafournoux P, and Bruhat A (2013). The eIF2α/ATF4 pathway is essential for stress-induced autophagy gene expression. Nucleic Acids Res 41, 7683–7699. 10.1093/nar/gkt563. [PubMed: 23804767]

Berge K.V. den, Bézieux H.R. de, Street K, Saelens W, Cannoodt R, Saeys Y, Dudoit S, and Clement L (2020). Trajectory-based differential expression analysis for single-cell sequencing data. Nat Commun 11, 1201. 10.1038/s41467-020-14766-3. [PubMed: 32139671]

Berlanga JJ, Herrero S, and Haro C. de (1998). Characterization of the Hemin-sensitive Eukaryotic Initiation Factor 2α Kinase from Mouse Nonerythroid Cells*. J Biol Chem 273, 32340–32346. 10.1074/jbc.273.48.32340. [PubMed: 9822714]

Berthenet K, Ferrer C, Fanfone D, Popgeorgiev N, Neves D, Bertolino P, Gibert B, Hernandez-Vargas H, and Ichim G (2020). Failed Apoptosis Enhances Melanoma Cancer Cell Aggressiveness. Cell Reports 31, 107731. 10.1016/j.celrep.2020.107731. [PubMed: 32521256]

Bhola P, and Letai A (2016). Mitochondria—Judges and executioners of cell death sentences. Mol. Cell 61, 695–704. [PubMed: 26942674]

Bialk P, Wang Y, Banas K, and Kmiec EB (2018). Functional Gene Knockout of NRF2 Increases Chemosensitivity of Human Lung Cancer A549 cells in vitro and in a Xenograft Mouse Model. Mol Ther - Oncolytics 11, 75–89. 10.1016/j.omto.2018.10.002. [PubMed: 30505938]

Bild AH, Yao G, Chang JT, Wang Q, Potti A, Chasse D, Joshi M-B, Harpole D, Lancaster JM, Berchuck A, et al. (2006). Oncogenic pathway signatures in human cancers as a guide to targeted therapies. Nature 439, 353–357. 10.1038/nature04296. [PubMed: 16273092]

Brasacchio D, Busuttil RA, Noori T, Johnstone RW, Boussioutas A, and Trapani JA (2018). Down-regulation of a pro-apoptotic pathway regulated by PCAF/ADA3 in early stage gastric cancer. Cell Death Dis 9, 442. 10.1038/s41419-018-0470-8. [PubMed: 29670108]

Broad-Institute (2019). Picard toolkit (http://broadinstitute.github.io/picard/).

Busuttil RA, George J, Tothill RW, Ioculano K, Kowalczyk A, Mitchell C, Lade S, Tan P, Haviv I, and Boussioutas A (2014). A Signature Predicting Poor Prognosis in Gastric and Ovarian Cancer Represents a Coordinated Macrophage and Stromal Response. Clin Cancer Res 20, 2761–2772. 10.1158/1078-0432.ccr-13-3049. [PubMed: 24658156]

Caserta TM, Smith AN, Gultice AD, Reedy MA, and Brown TL (2003). Q-VD-OPh, a broad spectrum caspase inhibitor with potent antiapoptotic properties. Apoptosis 8, 345–352. 10.1023/a:1024116916932. [PubMed: 12815277]

Chen J, Li Y, Yu T-S, McKay RM, Burns DK, Kernie SG, and Parada LF (2012). A restricted cell population propagates glioblastoma growth after chemotherapy. Nature 488, 522–526. 10.1038/nature11287. [PubMed: 22854781]

Colell A, Ricci J-E, Tait S, Milasta S, Maurer U, Bouchier-Hayes L, Fitzgerald P, Guio-Carrion A, Waterhouse NJ, Li CW, et al. (2007). GAPDH and Autophagy Preserve Survival after Apoptotic Cytochrome c Release in the Absence of Caspase Activation. Cell 129, 983–997. 10.1016/j.cell.2007.03.045. [PubMed: 17540177]

Condon KJ, Orozco JM, Adelmann CH, Spinelli JB, Helm P.W. van der, Roberts JM, Kunchok T, and Sabatini DM (2021). Genome-wide CRISPR screens reveal multitiered mechanisms through which mTORC1 senses mitochondrial dysfunction. Proc Natl Acad Sci USA 118, e2022120118. 10.1073/pnas.2022120118. [PubMed: 33483422]

Costa-Mattioli M, and Walter P (2020). The integrated stress response: From mechanism to disease. Science 368, eaat5314. 10.1126/science.aat5314. [PubMed: 32327570]

Crawford RR, Prescott ET, Sylvester CF, Higdon AN, Shan J, Kilberg MS, and Mungrue IN (2015). Human CHAC1 Protein Degrades Glutathione, and mRNA Induction Is Regulated by

the Transcription Factors ATF4 and ATF3 and a Bipartite ATF/CRE Regulatory Element*. J Biol Chem 290, 15878–15891. 10.1074/jbc.m114.635144. [PubMed: 25931127]

Dey S, Sayers CM, Verginadis II, Lehman SL, Cheng Y, Cerniglia GJ, Tuttle SW, Feldman MD, Zhang PJL, Fuchs SY, et al. (2015). ATF4-dependent induction of heme oxygenase 1 prevents anoikis and promotes metastasis. J Clin Invest 125, 2592–2608. 10.1172/jci78031. [PubMed: 26011642]

Dobin A, and Gingeras TR (2015). Mapping RNA-seq Reads with STAR. Curr Protoc Bioinform 51, 11.14.1–11.14.19. 10.1002/0471250953.bi1114s51.

Erler JT, Cawthorne CJ, Williams KJ, Koritzinsky M, Wouters BG, Wilson C, Miller C, Demonacos C, Stratford IJ, and Dive C (2004). Hypoxia-Mediated Down-Regulation of Bid and Bax in Tumors Occurs via Hypoxia-Inducible Factor 1-Dependent and -Independent Mechanisms and Contributes to Drug Resistance. Mol Cell Biol 24, 2875–2889. 10.1128/mcb.24.7.2875-2889.2004. [PubMed: 15024076]

Feng D, Amgalan D, Singh R, Wei J, Wen J, Wei TP, McGraw TE, Kitsis RN, and Pessin JE (2018). SNAP23 regulates BAX-dependent adipocyte programmed cell death independently of canonical macroautophagy. J Clin Invest 128, 3941–3956. 10.1172/jci99217. [PubMed: 30102258]

Fessler E, Eckl E-M, Schmitt S, Mancilla I, Meyer-Bender MF, Hanf M, Philippou-Massier J, Krebs S, Zischka H, and Jae LT (2020). A pathway coordinated by DELE1 relays mitochondrial stress to the cytosol. Nature 579, 1–5. 10.1038/s41586-020-2076-4.

Fox DB, Garcia NG, McKinney BJ, Lupo R, Noteware LC, Newcomb R, Liu J, Locasale JW, Hirschey MD, and Alvarez JV (2020). NRF2 activation promotes the recurrence of dormant tumour cells through regulation of redox and nucleotide metabolism. Nat Metabolism 2, 318–334. 10.1038/s42255-020-0191-z.

García-Jiménez C, and Goding CR (2019). Starvation and Pseudo-Starvation as Drivers of Cancer Metastasis through Translation Reprogramming. Cell Metab 29, 254–267. 10.1016/j.cmet.2018.11.018. [PubMed: 30581118]

Garrido C, Galluzzi L, Brunet M, Puig PE, Didelot C, and Kroemer G (2006). Mechanisms of cytochrome c release from mitochondria. Cell Death Differ 13, 1423–1433. 10.1038/sj.cdd.4401950. [PubMed: 16676004]

Goldman MJ, Craft B, Hastie M, Repečka K, McDade F, Kamath A, Banerjee A, Luo Y, Rogers D, Brooks AN, et al. (2020). Visualizing and interpreting cancer genomics data via the Xena platform. Nat Biotechnol 38, 675–678. 10.1038/s41587-020-0546-8. [PubMed: 32444850]

Guan J-J, Zhang X-D, Sun W, Qi L, Wu J-C, and Qin Z-H (2015). DRAM1 regulates apoptosis through increasing protein levels and lysosomal localization of BAX. Cell Death Dis 6, e1624–e1624. 10.1038/cddis.2014.546. [PubMed: 25633293]

Guedj M, Marisa L, Reynies A. de, Orsetti B, Schiappa R, Bibeau F, MacGrogan G, Lerebours F, Finetti P, Longy M, et al. (2012). A refined molecular taxonomy of breast cancer. Oncogene 31, 1196–1206. 10.1038/onc.2011.301. [PubMed: 21785460]

Guo X, Aviles G, Liu Y, Tian R, Unger BA, Lin Y-HT, Wiita AP, Xu K, Correia AM, and Kampmann M (2020). Mitochondrial stress is relayed to the cytosol by an OMA1–DELE1–HRI pathway. Nature 579, 427–432. 10.1038/s41586-020-2078-2. [PubMed: 32132707]

Győrffy B (2021). Survival analysis across the entire transcriptome identifies biomarkers with the highest prognostic power in breast cancer. Comput Struct Biotechnology J 19, 4101–4109. 10.1016/j.csbj.2021.07.014.

Győrffy B, Lánczky A, and Szállási Z (2012). Implementing an online tool for genome-wide validation of survival-associated biomarkers in ovarian-cancer using microarray data from 1287 patients. Endocr-Relat Cancer 19, 197–208. 10.1530/erc-11-0329. [PubMed: 22277193]

Haefen C. von, Gillissen B, Hemmati PG, Wendt J, Güner D, Mrozek A, Belka C, Dörken B, and Daniel PT (2004). Multidomain Bcl-2 homolog Bax but not Bak mediates synergistic induction of apoptosis by TRAIL and 5-FU through the mitochondrial apoptosis pathway. Oncogene 23, 8320–8332. 10.1038/sj.onc.1207971. [PubMed: 15467752]

Hangauer MJ, Viswanathan VS, Ryan MJ, Bole D, Eaton JK, Matov A, Galeas J, Dhruv HD, Berens ME, Schreiber SL, et al. (2017). Drug-tolerant persister cancer cells are vulnerable to GPX4 inhibition. Nature 551, 247–250. 10.1038/nature24297. [PubMed: 29088702]

Hao Z, Duncan GS, Chang C-C, Elia A, Fang M, Wakeham A, Okada H, Calzascia T, Jang Y, You-Ten A, et al. (2005). Specific Ablation of the Apoptotic Functions of Cytochrome c Reveals a Differential Requirement for Cytochrome c and Apaf-1 in Apoptosis. Cell 121, 579–591. 10.1016/j.cell.2005.03.016. [PubMed: 15907471]

Heckl D, Kowalczyk MS, Yudovich D, Belizaire R, Puram RV, McConkey ME, Thielke A, Aster JC, Regev A, and Ebert BL (2014). Generation of mouse models of myeloid malignancy with combinatorial genetic lesions using CRISPR-Cas9 genome editing. Nat Biotechnol 32, 941–946. 10.1038/nbt.2951. [PubMed: 24952903]

Heimer S, Knoll G, Schulze-Osthoff K, and Ehrenschwender M (2019). Raptinal bypasses BAX, BAK, and BOK for mitochondrial outer membrane permeabilization and intrinsic apoptosis. Cell Death Dis 10, 556. 10.1038/s41419-019-1790-z. [PubMed: 31324752]

Hetz C, Axten JM, and Patterson JB (2019). Pharmacological targeting of the unfolded protein response for disease intervention. Nat Chem Biol 15, 764–775. 10.1038/s41589-019-0326-2. [PubMed: 31320759]

Ichim G, and Tait SWG (2016). A fate worse than death: apoptosis as an oncogenic process. Nat Rev Cancer 16, 539–548. 10.1038/nrc.2016.58. [PubMed: 27364482]

Igarashi J, Murase M, Iizuka A, Pichierri F, Martinkova M, and Shimizu T (2008). Elucidation of the Heme Binding Site of Heme-regulated Eukaryotic Initiation Factor 2α Kinase and the Role of the Regulatory Motif in Heme S ensing by Spectroscopic and Catalytic Studies of Mutant Proteins. J Biol Chem 283, 18782–18791. 10.1074/jbc.m801400200. [PubMed: 18450746]

Inguaggiato P, Gonzalez-Michaca L, Croatt AJ, Haggard JJ, Alam J, and Nath KA (2001). Cellular overexpression of heme oxygenase-1 up-regulates p21 and confers resistance to apoptosis. Kidney Int 60, 2181–2191. 10.1046/j.1523-1755.2001.00046.x. [PubMed: 11737592]

Isobe T, Onn A, Morgensztern D, Jacoby JJ, Wu W, Shintani T, Itasaka S, Shibuya K, Koo PJ, O'Reilly MS, et al. (2013). Evaluation of Novel Orthotopic Nude Mouse Models for Human Small-Cell Lung Cancer. J Thorac Oncol 8, 140–146. 10.1097/jto.0b013e3182725ff9. [PubMed: 23328546]

Kale J, Osterlund EJ, and Andrews DW (2018). BCL-2 family proteins: changing partners in the dance towards death. Cell Death and Differentiation 25, 65–80. 10.1038/cdd.2017.186. [PubMed: 29149100]

Kalkavan H, and Green DR (2018). MOMP, cell suicide as a BCL-2 family business. Cell Death Differ 25, 46–55. 10.1038/cdd.2017.179. [PubMed: 29053143]

Kim K-H, Jeong J-Y, Surh Y-J, and Kim K-W (2010). Expression of stress-response ATF3 is mediated by Nrf2 in astrocytes. Nucleic Acids Res 38, 48–59. 10.1093/nar/gkp865. [PubMed: 19864258]

Kotschy A, Szlavik Z, Murray J, Davidson J, Maragno AL, Toumelin-Braizat G, Chanrion M, Kelly GL, Gong J-NN, Moujalled DM, et al. (2016). The MCL1 inhibitor S63845 is tolerable and effective in diverse cancer models. Nature 538, 477–482. 10.1038/nature19830. [PubMed: 27760111]

Krueger F, James F, Ewels P, Afyounian E, and Schuster-Boeckler, & B. (2021). FelixKrueger/TrimGalore: v0.6.7 - DOI via Zenodo (0.6.7). Zenodo.

Kuida K, Haydar TF, Kuan C-Y, Gu Y, Taya C, Karasuyama H, Su MS-S, Rakic P, and Flavell RA (1998). Reduced Apoptosis and Cytochrome c–Mediated Caspase Activation in Mice Lacking Caspase 9. Cell 94, 325–337. 10.1016/s0092-8674(00)81476-2. [PubMed: 9708735]

Lartigue L, Kushnareva Y, Seong Y, Lin H, Faustin B, and Newmeyer DD (2009). Caspaseindependent Mitochondrial Cell Death Results from Loss of Respiration, Not Cytotoxic Protein Release. Mol Biol Cell 20, 4871–4884. 10.1091/mbc.e09-07-0649. [PubMed: 19793916]

Li B, and Dewey CN (2011). RSEM: accurate transcript quantification from RNA-Seq data with or without a reference genome. Bmc Bioinformatics 12, 323–323. 10.1186/1471-2105-12-323. [PubMed: 21816040]

Li K, Li Y, Shelton JM, Richardson JA, Spencer E, Chen ZJ, Wang X, and Williams RS (2000). Cytochrome c Deficiency Causes Embryonic Lethality and Attenuates Stress-Induced Apoptosis. Cell 101, 389–399. 10.1016/s0092-8674(00)80849-1. [PubMed: 10830166]

Liberzon A, Birger C, Thorvaldsdóttir H, Ghandi M, Mesirov JP, and Tamayo P (2015). The Molecular Signatures Database Hallmark Gene Set Collection. Cell Syst 1, 417–425. 10.1016/j.cels.2015.12.004. [PubMed: 26771021]

Liu X, Kim C, Yang J, Jemmerson R, and Wang X (1996). Induction of apoptotic program in cell-free extracts: requirement for dATP and cytochrome c.

Liu X, He Y, Li F, Huang Q, Kato TA, Hall RP, and Li C-Y (2015). Caspase-3 Promotes Genetic Instability and Carcinogenesis. Mol Cell 58, 284–296. 10.1016/j.molcel.2015.03.003. [PubMed: 25866249]

Lopez J, Bessou M, Riley JS, Giampazolias E, Todt F, Rochegüe T, Oberst A, Green DR, Edlich F, Ichim G, et al. (2016). Mito-priming as a method to engineer Bcl-2 addiction. Nat Commun 7, 10538. 10.1038/ncomms10538. [PubMed: 26833356]

Love MI, Huber W, and Anders S (2014). Moderated estimation of fold change and dispersion for RNA-Seq data with DESeq2. Biorxiv 002832. 10.1101/002832.

Magnúsdóttir E, Dietmann S, Murakami K, Günesdogan U, Tang F, Bao S, Diamanti E, Lao K, Gottgens B, and Surani MA (2013). A tripartite transcription factor network regulates primordial germ cell specification in mice. Nat Cell Biol 15, 905–915. 10.1038/ncb2798. [PubMed: 23851488]

Maynard A, McCoach CE, Rotow JK, Harris L, Haderk F, Kerr DL, Yu EA, Schenk EL, Tan W, Zee A, et al. (2020). Therapy-Induced Evolution of Human Lung Cancer Revealed by Single-Cell RNA Sequencing. Cell 182, 1232–1251.e22. 10.1016/j.cell.2020.07.017. [PubMed: 32822576]

McStay GP, and Green DR (2014). Preparation of Cytosolic Extracts and Activation of Caspases by Cytochrome c. Cold Spring Harb Protoc 2014, pdb.prot080275. 10.1101/pdb.prot080275.

Melber A, and Haynes CM (2018). UPRmt regulation and output: a stress response mediated by mitochondrial-nuclear communication. Cell Res 28, 281–295. 10.1038/cr.2018.16. [PubMed: 29424373]

Merino D, Kelly GL, Lessene G, Wei AH, Roberts AW, and Strasser A (2018). BH3-Mimetic Drugs: Blazing the Trail for New Cancer Medicines. Cancer Cell 34, 879–891. 10.1016/j.ccell.2018.11.004. [PubMed: 30537511]

Miksanova M, Igarashi J, Minami M, Sagami I, Yamauchi S, Kurokawa H, and Shimizu T (2006). Characterization of Heme-Regulated eIF2α Kinase: Roles of the N-Terminal Domain in the Oligomeric State, Heme Binding, Catalysis, and Inhibition. Biochemistry-Us 45, 9894–9905. 10.1021/bi060556k.

Miles MA, and Hawkins CJ (2017). Executioner caspases and CAD are essential for mutagenesis induced by TRAIL or vincristine. Cell Death Dis 8, e3062–e3062. 10.1038/cddis.2017.454. [PubMed: 28981092]

Nagy Á, Munkácsy G, and Győrffy B (2021). Pancancer survival analysis of cancer hallmark genes. Sci Rep-Uk 11, 6047. 10.1038/s41598-021-84787-5.

Nieto MA (2011). The Ins and Outs of the Epithelial to Mesenchymal Transition in Health and Disease. Annu Rev Cell Dev Bi 27, 347–376. 10.1146/annurev-cellbio-092910-154036.

Niture SK, and Jaiswal AK (2012). Nrf2 Protein Up-regulates Antiapoptotic Protein Bcl-2 and Prevents Cellular Apoptosis. Journal of Biological Chemistry 287, 9873–9886. 10.1074/jbc.M111.312694. [PubMed: 22275372]

Oberst A, Ichim G, and Tait SWG (2016). Mitochondria and Cell Death. In Mitochondria and Cell Death, Hockenbery DM, ed. (Humana Press), pp. 213–226.

Okimoto RA, Breitenbuecher F, Olivas VR, Wu W, Gini B, Hofree M, Asthana S, Hrustanovic G, Flanagan J, Tulpule A, et al. (2017). Inactivation of Capicua drives cancer metastasis. Nat Genet 49, 87–96. 10.1038/ng.3728. [PubMed: 27869830]

Oren Y, Tsabar M, Cuoco MS, Amir-Zilberstein L, Cabanos HF, Hütter J-C, Hu B, Thakore PI, Tabaka M, Fulco CP, et al. (2021). Cycling cancer persister cells arise from lineages with distinct programs. Nature 596, 576–582. 10.1038/s41586-021-03796-6. [PubMed: 34381210]

Pakos-Zebrucka K, Koryga I, Mnich K, Ljujic M, Samali A, and Gorman AM (2016). The integrated stress response. EMBO Reports 17, 1374–1395. 10.15252/embr.201642195. [PubMed: 27629041]

Paoli P, Giannoni E, and Chiarugi P (2013). Anoikis molecular pathways and its role in cancer progression. Biochimica Et Biophysica Acta Bba - Mol Cell Res 1833, 3481–3498. 10.1016/j.bbamcr.2013.06.026.

Popgeorgiev N, Jabbour L, and Gillet G (2018). Subcellular Localization and Dynamics of the Bcl-2 Family of Proteins. Frontiers Cell Dev Biology 6. 10.3389/fcell.2018.00013.

Rabouw HH, Langereis MA, Anand AA, Visser LJ, Groot R.J. de, Walter P, and Kuppeveld F.J.M. van (2019). Small molecule ISRIB suppresses the integrated stress response within a defined window of activation. Proc Natl Acad Sci USA 116, 2097–2102. 10.1073/pnas.1815767116. [PubMed: 30674674]

Rafie-Kolpin M, Han A-P, and Chen J-J (2003). Autophosphorylation of Threonine 485 in the Activation Loop Is Essential for Attaining eIF2α Kinase Activity of HRI. Biochemistry-Us 42, 6536–6544. 10.1021/bi034005v.

Ran AF, Hsu PD, Wright J, Agarwala V, Scott DA, and Zhang F (2013). Genome engineering using the CRISPR-Cas9 system. Nature Protocols 8, 2281–2308. 10.1038/nprot.2013.143. [PubMed: 24157548]

Rehman SK, Haynes J, Collignon E, Brown KR, Wang Y, Nixon AML, Bruce JP, Wintersinger JA, Mer AS, Lo EBL, et al. (2021). Colorectal Cancer Cells Enter a Diapause-like DTP State to Survive Chemotherapy. Cell 184, 226–242.e21. 10.1016/j.cell.2020.11.018. [PubMed: 33417860]

Rème T, Hose D, Theillet C, and Klein B (2013). Modeling risk stratification in human cancer. Bioinformatics 29, 1149–1157. 10.1093/bioinformatics/btt124. [PubMed: 23493321]

Risso D, Ngai J, Speed TP, and Dudoit S (2014). Normalization of RNA-seq data using factor analysis of control genes or samples. Nat Biotechnol 32, 896–902. 10.1038/nbt.2931. [PubMed: 25150836]

Rzymski T, Milani M, Sin gleton DC, and Harris AL (2009). Role of ATF4 in regulation of autophagy and resistance to drugs and hypoxia. Cell Cycle 8, 3838–3847. 10.4161/cc.8.23.10086. [PubMed: 19887912]

Saelens X, Kalai M, and Vandenabeele P (2001). Translation Inhibition in Apoptosis Caspase-dependent PKR Activation and eIF2-α Phosphorylation. J Biol Chem 276, 41620–41628. 10.1074/jbc.m103674200. [PubMed: 11555640]

Shalem O, Sanjana NE, Hartenian E, Shi X, Scott DA, Mikkelsen TS, Heckl D, Ebert BL, Root DE, Doench JG, et al. (2014). Genome-Scale CRISPR-Cas9 Knockout Screening in Human Cells. Science 343, 84–87. 10.1126/science.1247005. [PubMed: 24336571]

Shen S, Vagner S, and Robert C (2020). Persistent Cancer Cells: The Deadly Survivors. Cell 183, 860–874. 10.1016/j.cell.2020.10.027. [PubMed: 33186528]

Singh R, Letai A, and Sarosiek K (2019). Regulation of apoptosis in health and disease: the balancing act of BCL-2 family proteins. Nat Rev Mol Cell Bio 20, 175–193. 10.1038/s41580-018-0089-8. [PubMed: 30655609]

Spandidos A, Wang X, Wang H, Dragnev S, Thurber T, and Seed B (2008). A comprehensive collection of experimentally validated primers for Polymerase Chain Reaction quantitation of murine transcript abundance. Bmc Genomics 9, 633. 10.1186/1471-2164-9-633. [PubMed: 19108745]

Spandidos A, Wang X, Wang H, and Seed B (2010). PrimerBank: a resource of human and mouse PCR primer pairs for gene expression detection and quantification. Nucleic Acids Res 38, D792–D799. 10.1093/nar/gkp1005. [PubMed: 19906719]

Street K, Risso D, Fletcher RB, Das D, Ngai J, Yosef N, Purdom E, and Dudoit S (2018). Slingshot: cell lineage and pseudotime inference for single-cell transcriptomics. Bmc Genomics 19, 477. 10.1186/s12864-018-4772-0. [PubMed: 29914354]

Stuart T, Butler A, Hoffman P, Hafemeister C, Papalexi E, Mauck WM, Hao Y, Stoeckius M, Smibert P, and Satija R (2019). Comprehensive Integration of Single-Cell Data. Cell 177, 1888–1902.e21. 10.1016/j.cell.2019.05.031. [PubMed: 31178118]

Sui X, Chen R, Wang Z, Huang Z, Kong N, Zhang M, Han W, Lou F, Yang J, Zhang Q, et al. (2013). Autophagy and chemotherapy resistance: a promising therapeutic target for cancer treatment. Cell Death Dis 4, e838–e838. 10.1038/cddis.2013.350. [PubMed: 24113172]

Szász AM, Lánczky A, Nagy Á, Förster S, Hark K, Green JE, Boussioutas A, Busuttil R, Szabó A, and Győrffy B (2016). Cross-validation of survival associated biomarkers in gastric cancer using transcriptomic data of 1,065 patients. Oncotarget 7, 49322–49333. 10.18632/oncotarget.10337. [PubMed: 27384994]

Tait SWG, and Green DR (2013). Mitochondrial Regulation of Cell Death. CSH Perspect Biol 5, a008706. 10.1101/cshperspect.a008706.

Tait S, Parsons MJ, Llambi F, Bouchier-Hayes L, Connell S, Muñoz-Pinedo C, and Green DR (2010). Resistance to Caspase-Independent Cell Death Requires Persistence of Intact Mitochondria. Developmental Cell 18, 802–813. 10.1016/j.devcel.2010.03.014. [PubMed: 20493813]

Tang D, Chen X, Kang R, and Kroemer G (2021). Ferroptosis: molecular mechanisms and health implications. Cell Res 31, 107–125. 10.1038/s41422-020-00441-1. [PubMed: 33268902]

Tang Z, Kang B, Li C, Chen T, and Zhang Z (2019). GEPIA2: an enhanced web server for large-scale expression profiling and interactive analysis. Nucleic Acids Res 47, W556–W560. 10.1093/nar/gkz430. [PubMed: 31114875]

Tian X, Zhang S, Zhou L, Seyhan AA, Borrero LH, Zhang Y, and El-Deiry WS (2021). Targeting the Integrated Stress Response in Cancer Therapy. Front Pharmacol 12, 747837. 10.3389/fphar.2021.747837. [PubMed: 34630117]

Tirosh I, Izar B, Prakadan, and Wadsworth M (2016). Dissecting the multicellular ecosystem of metastatic melanoma by single-cell RNA-seq. Science 10.1126/science.aad0501.

Ubellacker JM, Tasdogan A, Ramesh V, Shen B, Mitchell EC, Martin-Sandoval MS, Gu Z, McCormick ML, Durham AB, Spitz DR, et al. (2020). Lymph protects metastasizing melanoma cells from ferroptosis. Nature 585, 113–118. 10.1038/s41586-020-2623-z. [PubMed: 32814895]

Viswanathan VS, Ryan MJ, Dhruv HD, Gill S, Eichhoff OM, Seashore-Ludlow B, Kaffenberger SD, Eaton JK, Shimada K, Aguirre AJ, et al. (2017). Dependency of a therapy-resistant state of cancer cells on a lipid peroxidase pathway. Nature 547, 453–457. 10.1038/nature23007. [PubMed: 28678785]

Walter DM, Venancio OS, Buza EL, Tobias JW, Deshpande C, Gudiel AA, Kim-Kiselak C, Cicchini M, Yates TJ, and Feldser DM (2017). Systematic In Vivo Inactivation of Chromatin-Regulating Enzymes Identifies Setd2 as a Potent Tumor Suppressor in Lung Adenocarcinoma. Cancer Res 77, 1719–1729. 10.1158/0008-5472.can-16-2159. [PubMed: 28202515]

Wang C, and Youle R (2011). Predominant requirement of Bax for apoptosis in HCT116 cells is determined by Mcl-1's inhibitory effect on Bak. Oncogene 31, onc2011497. 10.1038/onc.2011.497.

Wang C-K, Yang S-C, Hsu S-C, Chang F-P, Lin Y-T, Chen S-F, Cheng C-L, Hsiao M, Lu FL, and Lu J (2017). CHAC2 is essential for self-renewal and glutathione maintenance in human embryonic stem cells. Free Radical Bio Med 113, 439–451. 10.1016/j.freeradbiomed.2017.10.345. [PubMed: 29054545]

Wang X, Spandidos A, Wang H, and Seed B (2012). PrimerBank: a PCR primer database for quantitative gene expression analysis, 2012 update. Nucleic Acids Res 40, D1144–D1149. 10.1093/nar/gkr1013. [PubMed: 22086960]

Yang JM, London IM, and Chen JJ (1992). Effects of hemin and porphyrin compounds on intersubunit disulfide formation of heme-regulated eIF-2 alpha kinase and the regulation of protein synthesis in reticulocyte lysates. J Biol Chem 267, 20519–20524. 10.1016/s0021-9258(19)88733-1. [PubMed: 1356981]

Yang T, Xu F, Sheng Y, Zhang W, and Chen Y (2016). A targeted proteomics approach to the quantitative analysis of ERK/Bcl-2-mediated anti-apoptosis and multi-drug resistance in breast cancer. Anal Bioanal Chem 408, 7491–7503. 10.1007/s00216-016-9847-7. [PubMed: 27510278]

Yang WS, SriRamaratnam R, Welsch ME, Shimada K, Skouta R, Viswanathan VS, Cheah JH, Clemons PA, Shamji AF, Clish CB, et al. (2014). Regulation of ferroptotic cancer cell death by GPX4. Cell 156, 317–331. 10.1016/j.cell.2013.12.010. [PubMed: 24439385]

Yu G, Wang L-G, Han Y, and He Q-Y (2012). clusterProfiler: an R Package for Comparing Biological Themes Among Gene Clusters. Omics J Integr Biology 16, 284–287. 10.1089/omi.2011.0118.

Zhang S, Macias-Garcia A, Ulirsch JC, Velazquez J, Butty VL, Levine SS, Sankaran VG, and Chen J-J (2019). HRI coordinates translation necessary for protein homeostasis and mitochondrial function in erythropoiesis. Elife 8, e46976. 10.7554/elife.46976. [PubMed: 31033440]

Highlights

- Sublethal BH3 mimetic treatment generates persisters in caspase-independent manner
- The persister phenotype implements a heightened metastatic potential
- Nuanced iMOMP and Cytochrome c release function as rheostat for ATF4 activation
- The persister phenotype is orchestrated by the Integrated Stress Response and ATF4

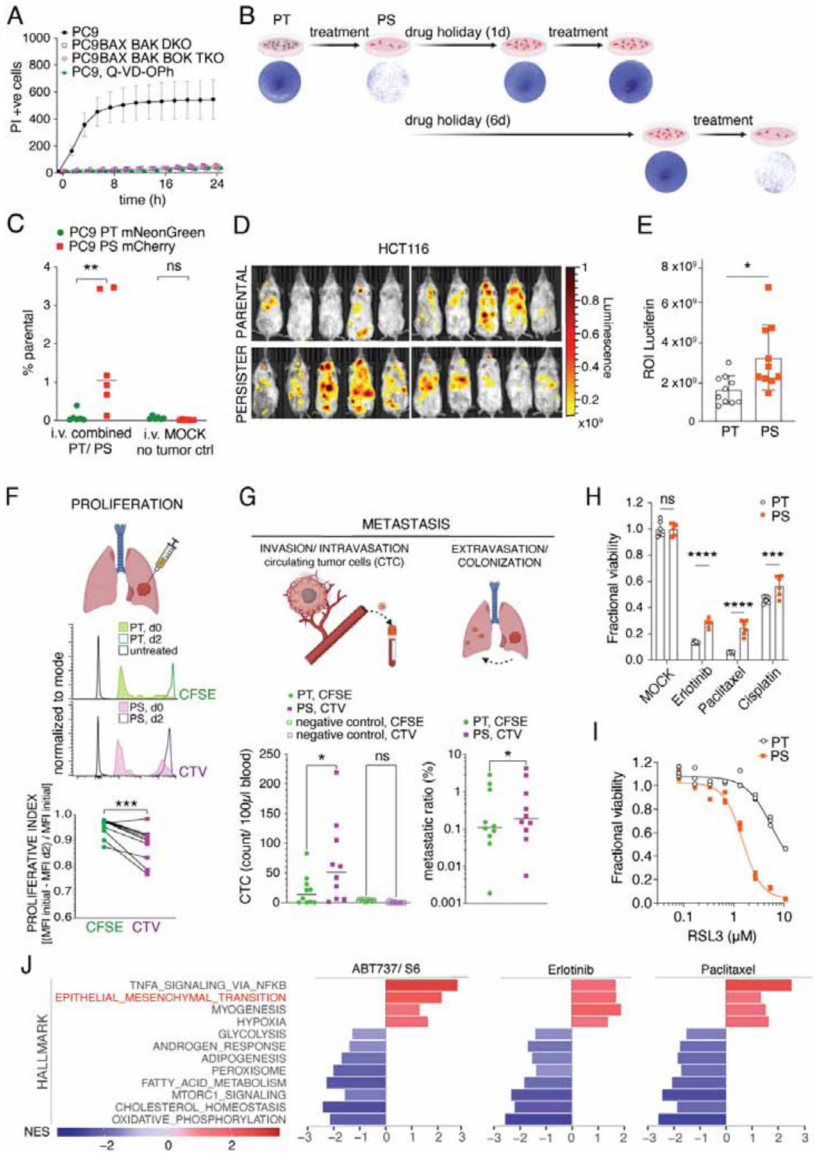

Figure 1. Targeting anti-apoptotic Bcl-2 proteins induces persister cells

(A) IncuCyte quantification during treatment with 1.5µM ABT737 and 3µM S6 of PC9 WT, PC9 *BAX*- and *BAK*-knockout (DKO), PC9 *BAX, BAK, BOK* TKO cells and PC9 WT cells co-treated with 40µM Q-VD-OPh (mean ± s.d. of n=3 samples/group).

(B) Clonogenic survival of cells treated or not with 1.5 µM ABT737 and 3µM S6 for 6h washed and replated, or treated and then re-seeded again after 1d or 6d and then retreated, washed, and released to growth. Representative of 3 independent experiments, n=3/group.

(C) Flow analysis of mNeonGreen positive PT or mCherry positive PS, from lungs of NSG mice 3 months after combined tail vein injection; n=6 lungs/group. MOCK, lungs without tumor injection.

(D) Intravital images and (E) ROI quantification of luciferase activity 3 weeks after injection of either PT or PS firefly-luciferase-expressing HCT116 cells (n=10 mice, mean ± s.d.). Representative of 2 independent experiments.

(F) Flow analysis of CFSE-labelled PT and CTV-labelled PS. Representative histograms on day 0 before injection and 48h after injection into left apical lungs of NSG mice. Proliferative index calculated by CFSE or CTV MFI signal loss from initial measurement to d2 (n=10 lungs/group, data from 2 pooled experiments).
(G) Flow analysis of CFSE-labelled PT and CTV-labelled PS from $RAG1^{-/-}$ mice (n=10). Left: Quantification of circulating tumor cells from right heart ventricle blood 48h after injection. Right: Metastatic ratio representing the ratio between cells in contralateral lung and primary injection site for PT or PS cells, respectively.
(H) Fractional viability of PC9 PT and PS treated with MOCK, Erlotinib 5μM, Paclitaxel 1μM or Cisplatin 10μM for 3d. N=6 samples/group.
(I) Fractional viability of PC9 PT and PS treated with RSL3 for 3d. N=3 samples/group.
(J) Hallmark pathways enriched across treatment regimens. Enriched pathways were defined as false discovery rate (FDR) <0.05. Normalized enrichment scores (NES) are shown. PS were generated by treatment with ABT737 1.5μM and S6 3μM for 6h, or Erlotinib 5μM for 3d or Paclitaxel 0.5μM for 3d. Statistical analysis by 2-way ANOVA (C, G left, H), unpaired student's t-test (E), paired student's t-test (F and G, right) respectively.
*P <0.05; **P <0.01; ***P <0.001; ****P <0.0001. See also Figure S1.

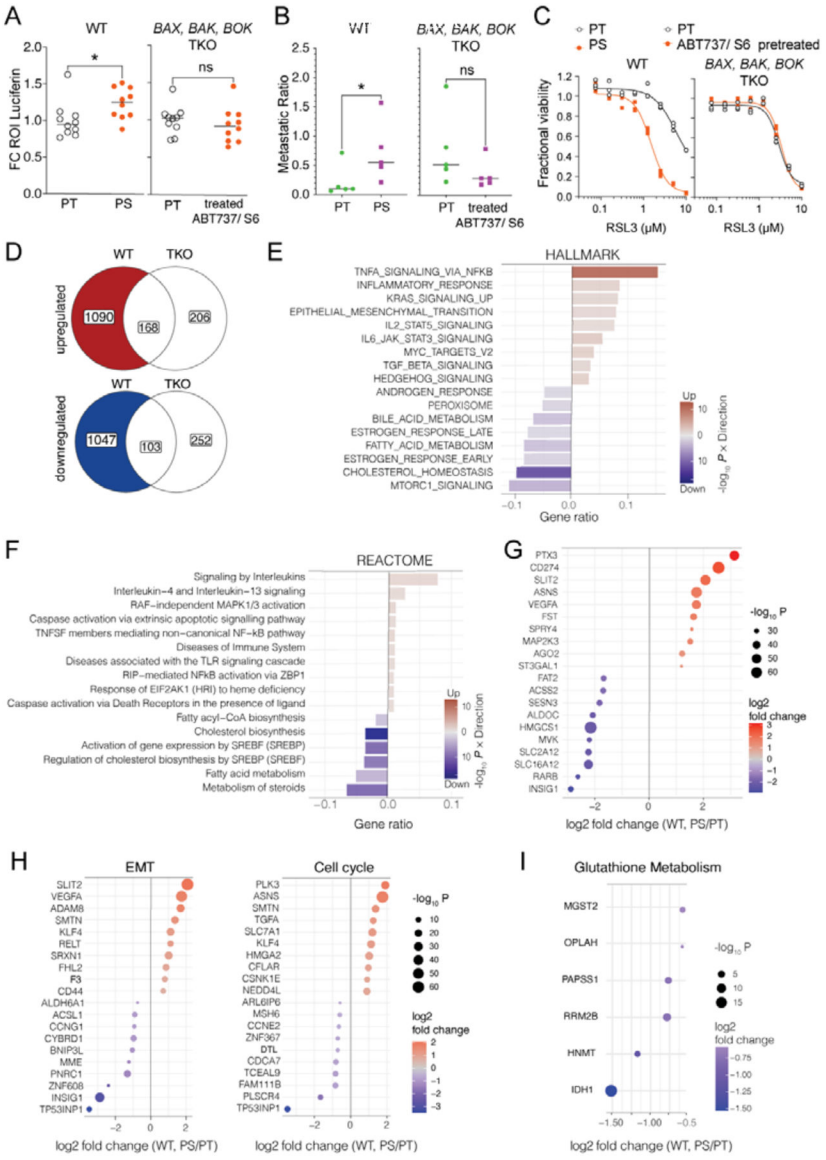

Figure 2. The persister phenotype depends largely on Bcl-2 effectors

(A) Luciferase activity 2d after injection of firefly luciferase-expressing PT versus PS WT or *BAX, BAK, BOK* TKO PC9 cells (n=10 mice/group, pooled from 2 independent experiments). All values are standardized to parental values within each experiment =1.

(B) Metastatic ratio of CFSE-labelled PT or CTV-labelled PS from PC9 WT or *BAX, BAK, BOK* TKO PC9 cells. N=5 mice/group (source data for WT from same experiment as Figure 1F).

(C) Fractional viability measured after 3d RSL3 treatment of PT and PS from WT or *BAX, BAK, BOK* TKO PC9 cells. Representative of 5 independent experiments shown, n=3 samples/group.

(D) Venn-Diagrams illustrating the number of differentially expressed genes (DEGs) in WT (PS/PT) but not in *BAX, BAK, BOK* TKO (ABT737, S6 treated/MOCK) PC9 cells. The

1090 DEGs that were only upregulated in WT but not in TKO cells (red) and the 1047 DEGs that were only downregulated in WT but not TKO cells (blue) were further analyzed (E to I).
(E) Enrichment analysis of Hallmark and (F) Reactome pathways shown as gene ratios of DEGs in WT (PS/PT) but not in *BAX, BAK, BOK* TKO (treated/MOCK) PC9 cells. The red bars show the genes up-regulated in PS and the blue down-regulated in PS. Enriched gene sets with adjusted p-value <0.05 are shown.
(G-I) Top 10 up- and downregulated DEGs in WT (PS/PT) but not in *BAX, BAK, BOK* TKO (treated/MOCK) PC9 cells. (source data as in E and F).
(D-I) DEGs have been defined as FC >1.5 and p-value <0.05. The gene sets were defined as a collection of gene sets in public databases.
Statistical analysis by unpaired student's t-test (A) or paired student's t-test (B). *P <0.05.
See also Figure S2.

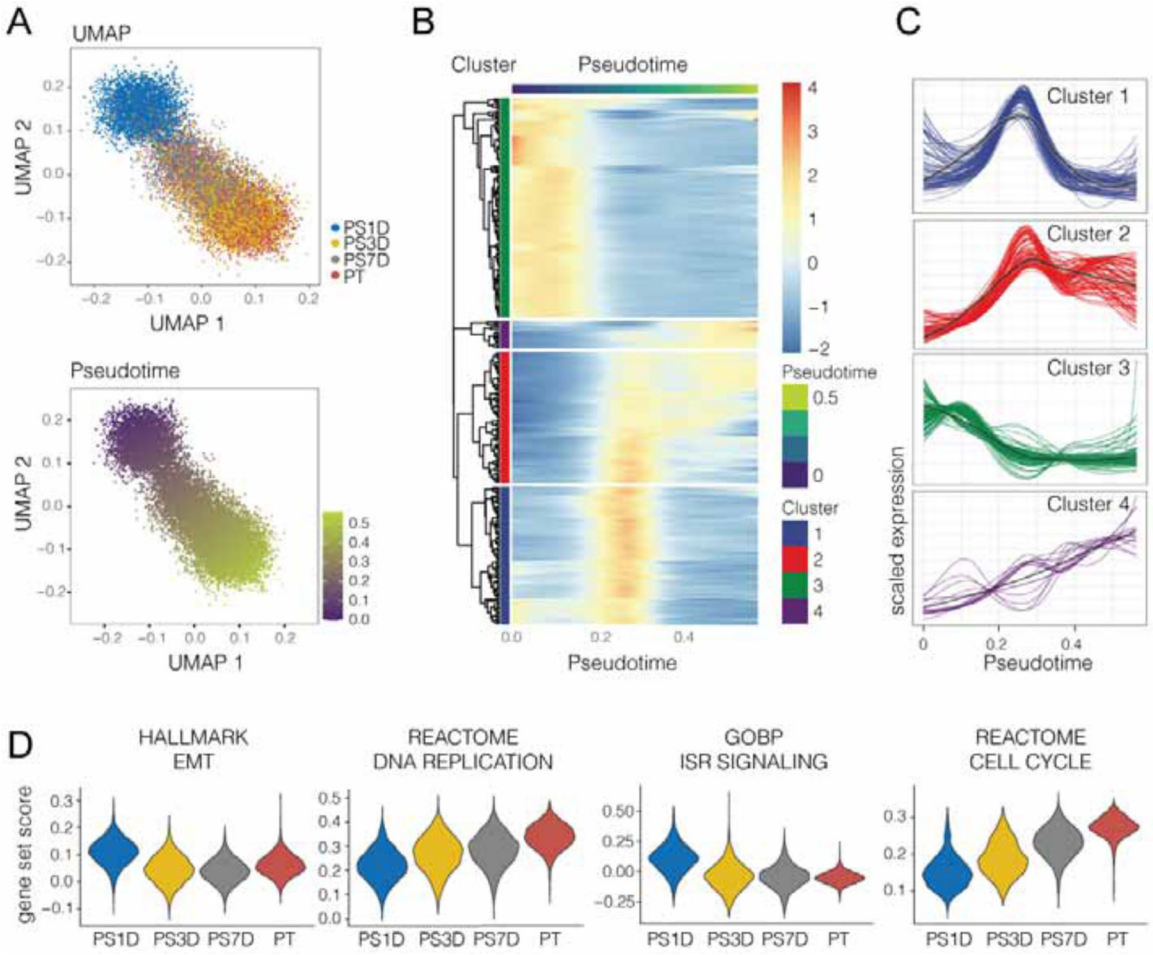

Figure 3. Transcriptomic trajectory analysis reveals transient ISR expression profile in BH3-mimetic persisters

(A) UMAP (upper) and Pseudotime (lower) single cell trajectories of PC9 PT and PS cells harvested after drug holiday of 1 day (PS1D), 3 days (PS3D) or 7 days (PS7D) and subjected to single cell RNAseq. The pseudotime was estimated using the Singleshot R package.

(B) Heatmap of differentially expressed genes along pseudotime (299 genes) identified using the tradeSeq R package. The expression was scaled and centered by gene, and the genes were clustered into four groups using hierarchical clustering.

(C) Scaled expression profiles of gene clusters along pseudotime.

(D) Violin plots visualizing gene set scores of selected gene sets.

See also Figure S2.

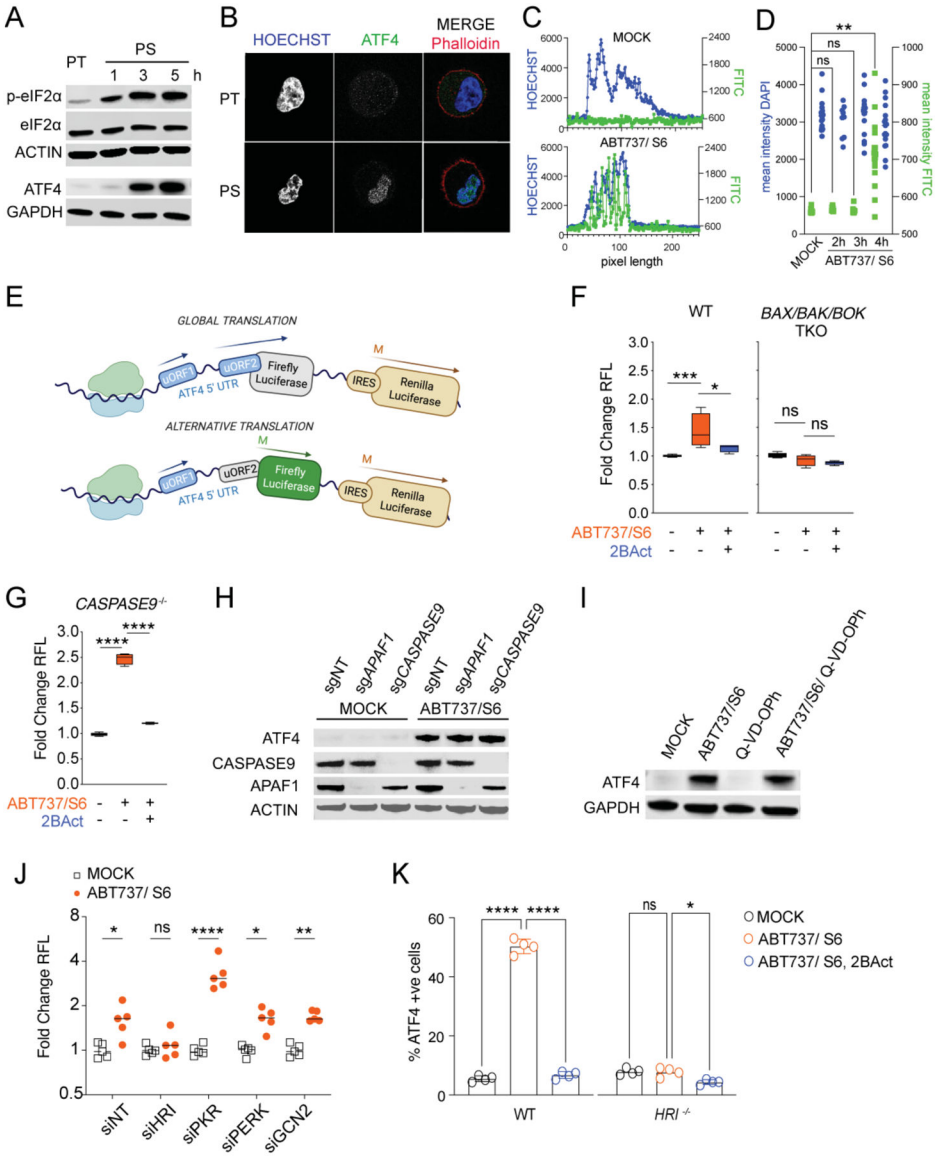

Figure 4. BH3 mimetics induce an ISR, dependent on Bcl-2 effectors but independent of caspase activation

(A) Immunoblot with the indicated antibodies of PC9 PT and PS, generated by treatment with ABT737 1.5μM and S6 3μM for the indicated times.

(B) Confocal microscopy images of PC9 PT and PS after 4h treatment with ABT737 and S6. Cells were stained for Hoechst (blue), ATF4 (green) and Phalloidin (red).

(C) Fluorescence intensity of immunofluorescence from (B) measured in one dimension across the cell through the nucleus. One representative of n=19 PT and n= 18 PS measurements shown.

(D) Mean intensity of immunofluorescence from (B) measured within the nuclear area in PT (n=19) and PS after 2h (n=9), 3h (n=15) or 4h (n=18) treatment. Dots indicate individual cells.

(E) Schematic representation of the luciferase-expressing ATF4 translation reporter construct and its activation under alternative translation conditions.

(F) Luciferase activity assay from (E) showing normalized firefly luciferase activity in PC9 WT and *BAX, BAK, BOK* TKO cells treated with ABT737 1μM and S6 2μM ± 2Bact 20μM. Data is shown as fold change of RFL compared to MOCK control (mean ± s.d. of n=3 samples/group).
(G) Same as (F) in *CASPASE9* KO PC9 cells (mean ± s.d. of n=3 samples/group).
(H) Immunoblot of endogenous ATF4, APAF1 and CASPASE9 in PC9 cells after transient expression of Cas9 and either sgNT, sg*APAF1* or sg*CASPASE9*. Cells were treated with ABT737 1μM and S6 2μM for 6h.
(I) Immunoblot of endogenous ATF4 in PC9 cells after treatment with ABT737 1μM and S6 2μM and QVD-OPh 10μM.
(J) Luciferase activity assay showing normalized firefly luciferase activity in PC9 cells expressing luciferase ATF4 translation reporter. Cells were silenced with siNT or siRNA for each of the EIF2α- kinases indicated and treated ± ABT737 1μM and S6 2μM for 6h. n=5 samples/group.
(K) Flow analysis of nuclear ATF4 after MOCK or ABT737 1.5μM and S6 3μM ± 2BAct 50μM treatment for 4h in WT or $HRI^{-/-}$ cells. N=4 samples/group.
Statistical analysis by unpaired student's t-test (D) or 2-way ANOVA (F, G, J and K). *P <0.05; **P <0.01; ***P <0.001; ****P <0.0001. See also Figure S3.

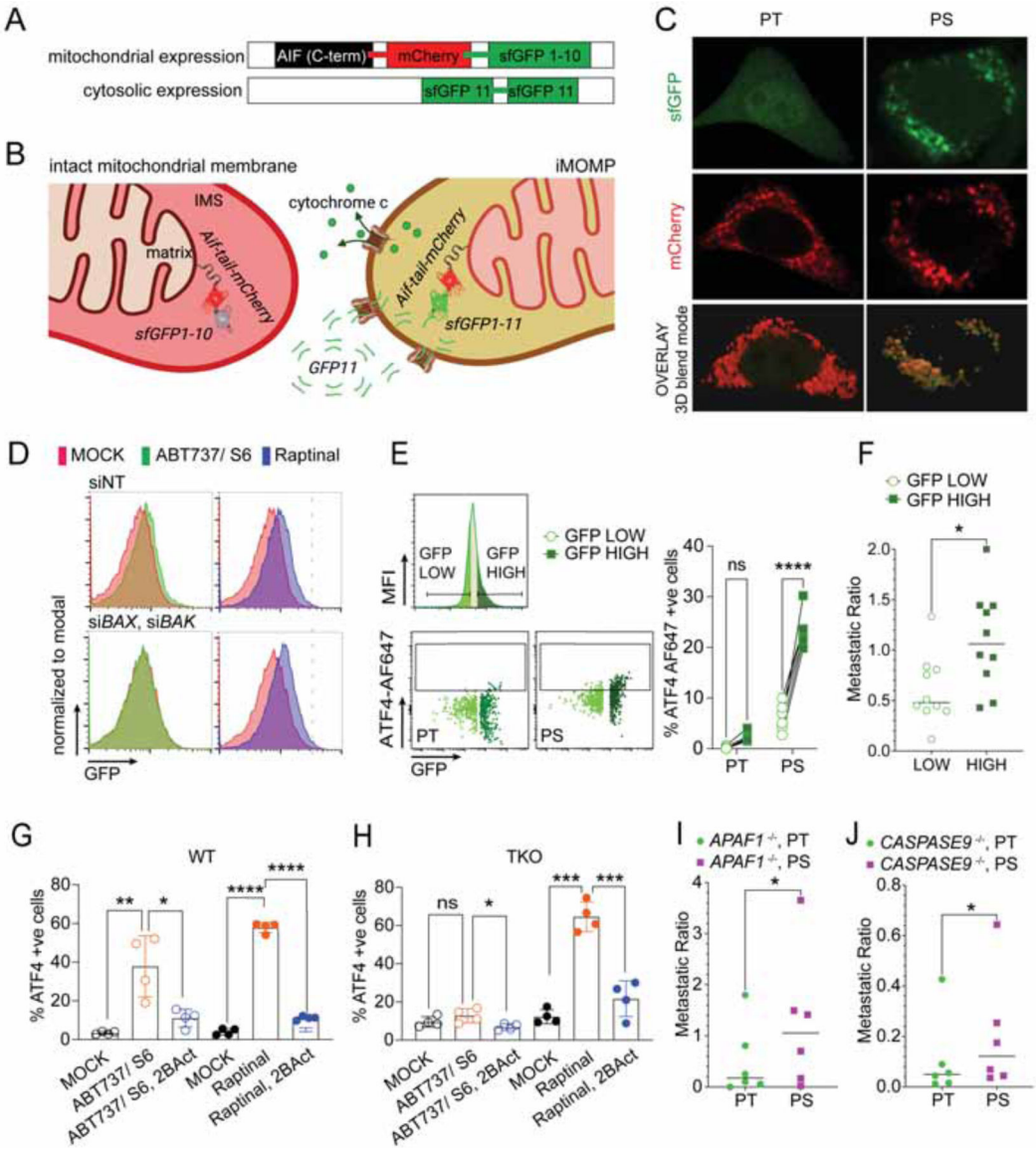

Figure 5. Engagement of sublethal MOMP is crucial for ISR activation

(A) Schematic representation of the mitochondrial and cytosolic expression system for the MOMP sensor and (B) its function upon MOMP.

(C) Confocal microscopy images of A549 PT and PS expressing the MOMP sensor system. PS were generated by 6h treatment with ABT737 1.5μM and S6 3μM and then released overnight before imaging. 3D blend mode image was generated with IMARIS.

(D) Flow analysis of A549 cells expressing the MOMP sensor. Cells were transfected with either non-targeted (siNT) or BAX and BAK targeting siRNA (si*BAX*, si*BAX*) and treated with MOCK, ABT737 5μM and S6 10μM or Raptinal 5μM. Representative histograms from n=3 samples/group are shown.

(E) Fow analysis of A549 PT and PS expressing the iMOMP sensor. Left upper panel: representative histogram showing strategy of gating GFP high (25%) and low (25%) cells. Left lower panels: dot plots showing cytosolic ATF4 and GFP in the two stratified groups.

Right panel: quantitation of ATF4 positive cells in PT or PS, GFP high and GFP low cells. N=6 samples/group. One representative of 2 independent experiments shown.

(F) Metastatic ratio representing the ratio between cells from the contralateral lung and primary injection site. Analysis of CTV-labelled PS from NSG mice was performed 2d after intrapulmonal injection of either GFP-high or GFP-low sorted PS cells respectively (n=10 mice/group).

(G-H) Flow analysis of nuclear ATF4 after MOCK or ABT737 1.5μM and S6 3μM or Raptinal 5μM ± 2BAct 50μM treatment for 4h in WT (G) or *BAX, BAK, BOK* TKO cells (H). Mean ± s.d. of n=4 samples/group are shown.

(I, J) Metastatic ratios between cells from the contralateral lung and primary injection site. Analysis of CFSE-labelled PT and CTV-labelled PS from $APAF1^{-/-}$ (I) or $CASP9^{-/-}$ (J) PC9 cells was performed 2d after intrapulmonal combined injection (n=6 mice/group). Statistical analysis was performed using unpaired student's t-test (F), 2-way ANOVA (E, G and H) or paired student's t-test (I and J). *P <0.05; **P <0.01; ***P <0.001; ****P <0.0001. See also Figure S3.

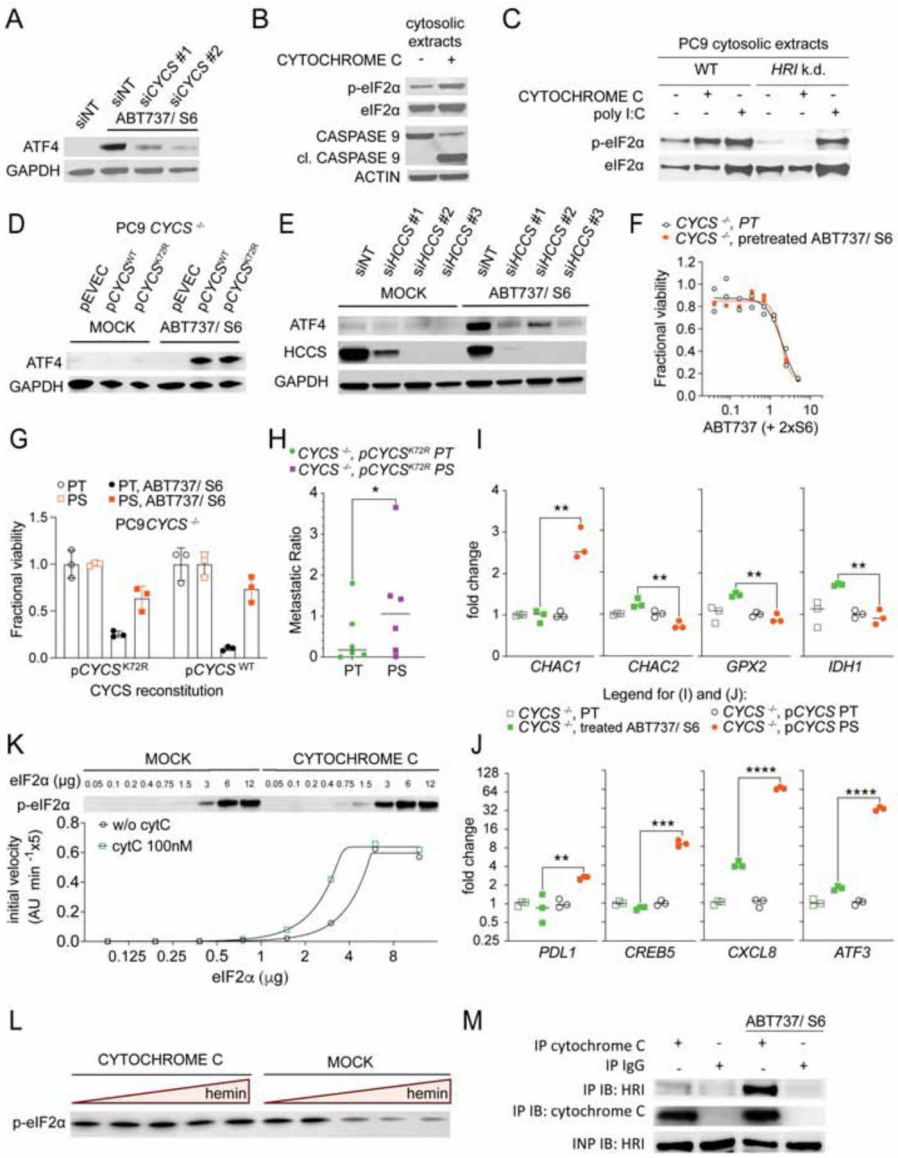

Figure 6. Cytochrome c activates HRI and engages the persister phenotype

(A) Immunoblot with the indicated antibodies of PC9 cells that had been transfected with non-targeting (siNT) or 2 different *CYCS* targeting siRNAs, and treated ± ABT737 1.5μM and S6 3μM for 4h. All samples were treated with Q-VD-OPh 20μM.

(B) Immunoblot of cytosolic extracts from PC9 cells treated ± 100nM bovine Cytochrome c for 30min in the presence of 50μM ATP.

(C) Immunoblot of cytosolic extracts from PC9 WT and HRI-silenced cells treated ± 100nM bovine Cytochrome c or 10μg/ml poly I:C for 30 min in the presence of 50μM ATP.

(D) Immunoblot with the indicated antibodies of PC9 $CYCS^{-/-}$ cells, reconstituted ± WT or K72R mutant *CYCS* and treated ± ABT737 1.5μM and S6 3μM for 4h. All samples were treated with Q-VD-OPh 20μM.

(E) Immunoblot with the indicated antibodies of PC9 cells that had been transfected with non-targeting (siNT) or different *HCCS*-targeting siRNAs and treated ± ABT737 1.5μM and S6 3μM for 4h. All samples were treated with Q-VD-Oph 20μM.

(F) Fractional viability of PT and BH3-mimetic survivors generated from PC9 *CYCS*$^{-/-}$ cells treated with a titration of ABT737 and S6. Mean ± s.d. of 3 samples. One representative of n=2 independent experiments shown.

(G) Fractional viability of PT and PS generated from PC9 *CYCS*$^{-/-}$ cells, reconstituted ± WT or K72R mutant *CYCS* and treated ± ABT737 1.5μM and S6 3μM. One representative of n=2 independent experiments shown.

(H) Metastatic ratio of PT and PS generated from PC9 *CYCS*$^{-/-}$ cells that had been reconstituted with *CYCS* K72R mutant (n=6 mice/group). Statistical analysis by paired student's t-test. *P <0.05.

(I) and (J) qPCR analysis of transcripts involved in glutathione metabolism (I) or diverse transcripts that have been identified as BCL2 effector protein dependent (J) of PT and PS generated from PC9 *CYCS*$^{-/-}$ cells, reconstituted ± WT *CYCS*. N=3 samples are shown. Statistical analysis was performed using unpaired student's t-test. **P <0.01, ***P <0.001; ****P <0.0001.

(K) Immunoblot and HRI enzyme kinetics in the presence or absence of Cytochrome c 100nm with recombinant proteins. One representative fitting curve from n=3 independent experiments shown.

(L) Immunoblot of in vitro kinase reaction with recombinant eIF2α and HRI, in the presence or absence of Cytochrome c and ± hemin titration (from 2μM max. to 3nM min., 1:5 dilutions in kinase buffer).

(M) Immunoprecipitation of endogenous Cytochrome c or IgG (negative control) from *APAF1* KO PC9 cells treated ± ABT737 and S6.

See also Figures S4 and S5.

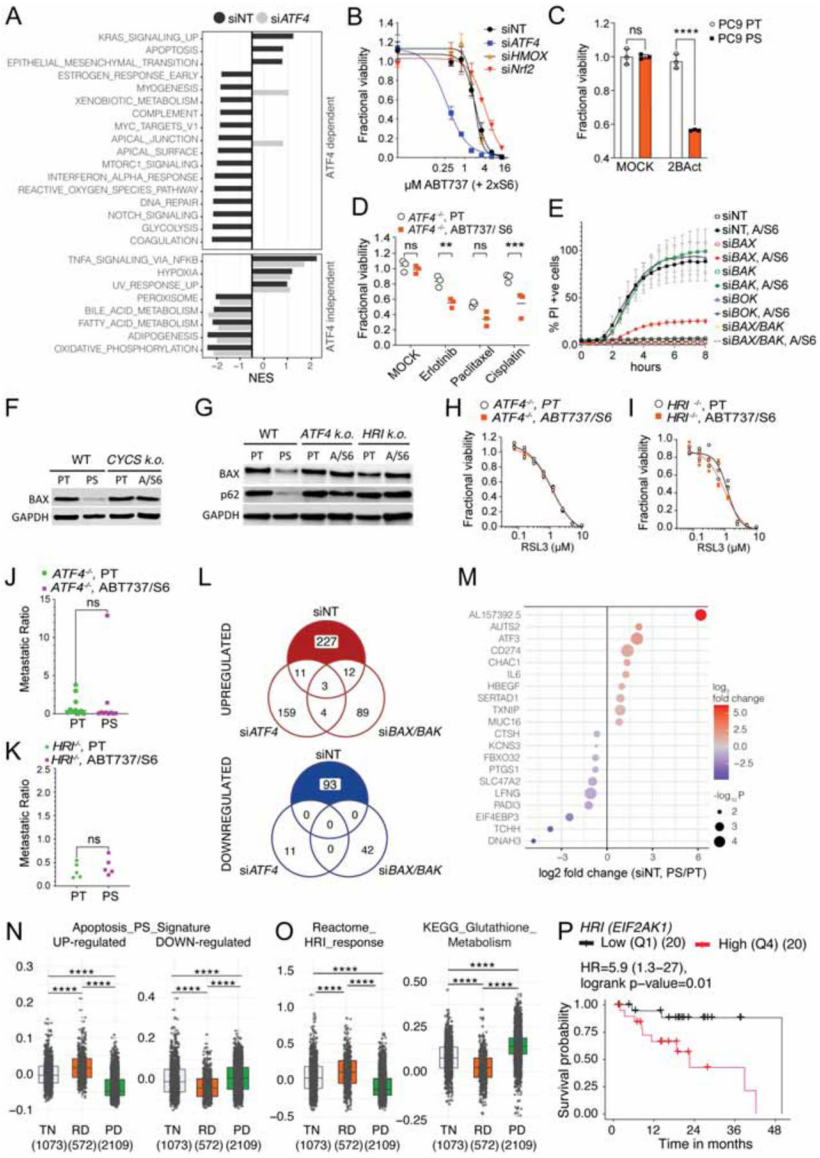

Figure 7. Cytochrome c – HRI – ATF4 axis drives the phenotype of persistence

(A) Cancer hallmarks pathway analysis in BH3-mimetic treated versus untreated cells significantly changed in siNT (PS/PT) but not si*ATF4* (ABT737, S6 treated/MOCK) PC9 cells.

(B) Fractional viability of PC9 cells that had been transfected with siNT, si*ATF4*, si*HMOX1* or si*NRF2*, and treated with a titration of ABT737 and S6. One representative of 2 independent experiments shown.

(C) Fractional viability of PC9 PT and PS that had been treated with 50μM of 2BAct. N=3 samples/group.

(D) Fractional viability of PT and BH3-mimetic survivors that were generated from *ATF4*$^{-/-}$ cells, and had been treated with MOCK, Erlotinib 5μM, Paclitaxel 1μM or Cisplatin 10μM for 3d. N=3 samples/group.

(E) IncuCyte quantification during treatment with ABT737 (1.5μM) and S6 (3μM) of PC9 cells transfected with siNT, si*BAX*, si*BAK*, si*BOK* or a combination of si*BAX* and si*BAK* WT. Data are mean ± s.d. of n=3 samples/group. One representative of 3 independent experiments is shown.
(F) Immunoblot of BAX in WT and *CYCS* KO cells treated ± ABT737 and S6.
(G) Immunoblot of BAX in WT and *ATF4* KO and *HRI* KO cells treated ± ABT737 and S6.
(H) Fractional viability of PT and BH3-mimetic survivors generated from PC9 $ATF4^{-/-}$ cells treated with a titration of RSL3. One representative of 7 independent experiments shown.
(I) Fractional viability of PT and BH3-mimetic survivors generated from PC9 $HRI^{-/-}$ cells treated with titration of RSL3. One representative of 6 independent experiments shown.
(J) Metastatic ratio of PT and BH3-mimetic survivors generated from PC9 $ATF4^{-/-}$ (n=10 mice/group).
(K) Metastatic ratio of PT and BH3-mimetic survivors generated from PC9 $HRI^{-/-}$ (n=5 mice/group), (same experiment as Figure 1E).
(L) Venn-Diagrams illustrating the number of differentially expressed genes (DEGs) in siNT (PS/PT), *siATF4* (ABT737, S6 treated/MOCK) or *siBAX/BAK* (ABT737, S6 treated/MOCK) PC9 cells. Numbers of up- and down-regulated genes are shown.
(M) DEGs dependent on ATF4 and BAX, BAK. Top 10 genes from 227 up- and 93 down-regulated DEGs that are significantly changed in siNT- but not si*ATF4*- or si*BAX*/*BAK*-silenced cells are depicted.
(N) Gene set score for an apoptosis signature generated with DEGs in PS and not PT that are dependent on ATF4 and BAX, BAK (see also M), that are up- or down-regulated in human lung cancers from patients which were treatment-naïve (TN, n=1073 samples), had residual disease (RD, n=572 samples) or had progressive disease (PD, n=2109 samples). The published data set is from Maynard *et al.*, 2020.
(O) Gene set score for Reactome HRI response and KEGG Glutathione metabolism gene set that were up- or down-regulated in human lung cancers from the data set in (N). Statistical analysis was performed using t-test ****P <0.0001.
(P) Kaplan Meier survival curve of patients with EGFR-mutant lung adenocarcinoma expressing high (4^{th} quartile) or low (1^{st} quartile) HRI from TCGA database lung adenocarcinoma (LUAD) cohort. Hazard ratio (HR) and p-value is indicated. N=20/group. Statistical analysis was performed using 2-way ANOVA (C and D) and paired student's t-test (J and K). **P <0.01, ***P <0.001; ****P <0.0001. See also Figures S6 and S7.

KEY RESOURCES TABLE

REAGENT or RESOURCE	SOURCE	IDENTIFIER
Antibodies		
Cytochrome C – AF 647	BioLegend	Cat# 612310, RRID:AB_2565241
CD45 – APC	BD	Cat# 559864 RRID:AB_398672
GAPDH (0411) HRP	Santa Cruz	Cat# sc-47724 HRP RRID:AB_627678
HRI (D-12)	Santa Cruz	Cat# sc-365239 RRID:AB_10843794
eIF2alpha	CST	Cat# 9722 RRID:AB_2230924
eIF2 pS51	Abcam	Cat# ab32157 RRID:AB_732117
ATF-4	CST	Cat# 11815 RRID:AB_2616025
HRI (D-12) (EIF2AK1)	Proteintech	Cat# 20499-1-AP RRID:AB_10697665
PKR (EIF2AK2)	Santa Cruz	Cat# sc6282 RRID:AB_628150
Perk (EIF2AK3)	CST	Cat# 3192 RRID:AB_2095847
GCN2 (EIF2AK4)	CST	Cat# 40457 RRID:AB_2799177
Nrf2	Santa Cruz	Cat# sc13032 RRID:AB_2263168
Heme Oxygenase 1 Antibody (A-3)	Santa Cruz	Cat# sc-136960 RRID:AB_2011613
GAPDH-HRP	Santa Cruz	Cat# sc47724-HRP RRID:AB_627678
β-Actin Antibody (C4) HRP	Santa Cruz	Cat# sc-47778 HRP RRID:AB_2714189
Caspase9	CST	Cat# 9502S RRID:AB_2068621
HCCS	Abcam	Cat# ab234874
APAF-1	CST	Cat# 5088S RRID:AB_10556958
BAX	CST	Cat# 2772 RRID:AB_10695870
BAK	CST	Cat# 3814 RRID:AB_2290287
BOK	Abcam	Cat# ab186745 RRID:AB_2728737
Cytochrome c (D18C7) Rabbit mAb	CST	Cat# 11940S RRID:AB_2637071
Amersham ECL Rabbit IgG, HRP-linked whole Ab (from donkey)	Amersham	Cat# NA934 RRID:AB_772206
Cytiva's Amersham ECL Mouse IgG, HRP-linked whole Ab (from sheep)	Amersham	Cat# NA931 RRID:AB_772210
Anti-NRF2 antibody [N2C2]	Genetex	Cat# GTX103322 RRID:AB_1950993
GFP-Booster Alexa Fluor® 488	Chromotek	Cat# gb2AF488 RRID:AB_2827573
RFP-Booster Alexa Fluor® 568	Chromotek	Cat# rb2AF568 RRID:AB_2827576
BODIPY™ 581/591 C11	Thermo Fisher	Cat# D3861
Cytochrome C	BD	Cat# 556432 RRID:AB_396416
GFP-Trap Magnetic Agarose	Chromotek	Cat# gtma-20 RRID:AB_2631358
p62/SQSTM1	Sigma	Cat# P0067 RRID:AB_1841064
Bacterial and Virus Strains		
NEB®10-beta Competent E.coli (High Efficiency)	NEB	Cat# C3019H
NEB 5-alpha Competent E.coli	NEB	Cat# C2987H
NEB® Stable Competent E.coli (High Efficiency)	NEB	Cat# C3040H

REAGENT or RESOURCE	SOURCE	IDENTIFIER
TOPO™ TA Cloning™ Kit for Sequencing, with One Shot™ TOP10 Chemically Competent E. coli	Thermo Fisher	Cat# K4575J10
Biological Samples		
-		
Chemicals, Peptides, a Recombinant Proteins		
ABT-737	MCE	Cat# HY-50907
S63845	MCE	Cat# HY-100741
ISRIB	MCE	Cat# HY-12495
2BAct	AOBIOUS	Cat# 2143542-28-1
Paclitaxel	MCE	Cat# HY-B0015
RSL3	Selleck Chemicals	Cat# S8155
Irinotecan	MCE	Cat# HY-16562
Erlotinib	Cayman	Cat# 10483
Vemurafenib (PLX4032)	Cayman	Cat# 10618
Raptinal	Millipore Sigma	Cat# SML1745
Digitonin	Sigma-Aldrich	Cat# D141
Eif2s1, His tagged human,recombinant	Sigma-Aldrich	Cat# SRP5232
Eif2ak1 (HRI) Human Protein	Thermo Scientific	Cat# PV5856
3X FLAG® Peptide	Sigma-Aldrich	Cat# F4799
AC DEVD AFC	Enzo Life Sciences	Cat# ALX260032M005
Cytochrome c from Saccharomyces cerevisiae	Sigma-Aldrich	Cat# C2436
Cytochrome C, equine	Sigma-Aldrich	Cat# C2506
Cytochrome C, bovine	Sigma-Aldrich	Cat# C2037
Liberase TM	Sigma-Aldrich	Cat# 5401119001
DNase I, Grade II, from bovine pancreas	Sigma-Aldrich	Cat# 10104159001
Corning® Matrigel® Basement Membrane Matrix, LDEV-Free	Corning	Cat# 356234
Deferoxamine mesylate salt	Sigma-Aldrich	Cat# D9533-1G
Critical Commercial Assays		
RNeasy Mini Kit	Qiagen	Cat#74104
Direct-zol RNA MicroPrep (200 Preps) w/ Zymo-Spin IC Columns (Capped)	Zymo Research	Cat# R2062
Intracellular Fixation & Permeabilization Buffer Set	BD	Cat# 554714
eBioscience Foxp3 / Transcription Factor Staining Buffer Set	Thermo Scientific	Cat# 00-5523-00
Dual-Luciferase Reporter 1000 Assay System	Promega	Cat# E1980
CellTiter-Glo Luminescent Cell Viability Assay	Promega	Cat# G7572
CellTrace™ CFSE Cell Proliferation Kit, for flow cytometry	Thermo Scientific	Cat# C34554
Cell Trace Violet	Thermo Scientific	Cat# C34557
Clarity™ Western ECL Substrate, 500 ml, 1705061	Bio-Rad	Cat# 1705061
Xt MES Running Buffer, 1610789	Bio-Rad	Cat# 1610789
20S Proteasome Lysis Buffer	CAYMAN Chemicals	Cat# 10011098

REAGENT or RESOURCE	SOURCE	IDENTIFIER
Lipofectamine 3000 Transfection Reagen	Thermo Scientific	Cat# L3000001
Fugene HD Transfection Reagent, Promega, FuGENE HD Transfection	Promega	Cat# E2311
ViaFect Transfection Reagent	Promega	Cat# E4981
Lipofectamine™ RNAiMAX Transfection Reagent	Therno Scientific	Cat# 13778075
Ercc RNA Spike-In Mix	Thermo Scientific	Cat# 4456740
pcDNA3.1/V5-His TOPO TA Expression Kit	Thermo Scientific	Cat# K480001
ANTI-FLAG® M2 Affinity Gel,purified immunoglobulin, buffered aqueous	Sigma-Aldrich	Cat# A2220
SYBR Green PCR Master Mix	Applied Biosystems	Cat#4309155
Chromium Next GEM Single Cell 3′ Library Kit v3.1 16 rxns	10X Genomics	PN-1000157
Chromium Next GEM Chip G Single Cell Kit, 16 rxns	10X Genomics	PN-100012
Mycoalert Detection kit	Lonza	Cat# LT07-318
EasySep Dead Cell Removal (Annexin V) kit	STEMCELL technologies	Cat# 17899
Next Seq 500/550 High Output Kit v2	Illumina	Cat#FC-404-2002
TruSeq Stranded mRNA kits	Illumina	Cat#20020595
Zombie Violet Viability Kit	Biolegend	Cat#423113
Deposited Data		
SuperSeries		GSE189639
bulk RNA-seq of parental and persister cells generated human cancer cells		GSE189625
scRNAseq of PC9 parental and persister cells		GSE189638
Experimental Models: Cell Lines		
H. sapiens: PC9	ATCC	
H. sapiens: HCT116	Richard Youle	
H. sapiens: HT29	ATCC	
H. sapiens: A549	Richard J. Webby, SJRH	
H. sapiens: H226	ATCC	
Experimental Models: Organisms/Strains		
NOD.Cg-Prkdcsscid Il2rgtm1Wjl/SzJ (NSG)	In house	
$Rag1^{-/-}$	In house	
Oligonucleotides		
sgRNA see Table S3	abm (Lopez et al., 2016; Shalem et al., 2014)	N/A
siRNA see Table S4	Dharmacon, IDT	N/A
qPCR primer see Table S5	Origene sequences, (Kim et al., 2010; Spandidos et al., 2008, 2010; Wang et al., 2012)	N/A
Recombinant DNA		
Piggybac expression system (inducible)	(Magnúsdóttir et al., 2013)	
pPB constitutive CMV	This paper	

REAGENT or RESOURCE	SOURCE	IDENTIFIER
pPB (puro)-mCherry	This paper	
pPB (puro)-mNeonGreen	This paper	
pPB (puro)_hUTR(ATF4) luci_IRES RenLuciferase	This paper	
pPB (puro) mitoV1 AifTail-mCh-GFP1-10	This paper	
pPB (Blast)	This paper	
pPB (Blast) 2xGFP11 (M3)	This paper	
pPB (Zeo)	This paper	
pPB (Zeo)_CYCS	This paper	
pPB (Zeo)_CYCS K72R	This paper	
pPB Luciferase-tdTomato	This paper	
pcDNA TOPO TA mClover	This paper	
pXG290 (HRI-mClover)	(Guo et al., 2020)	Addgene 141284
Px458 pSpCas9(BB)-2A-GFP	(Ran et al., 2013)	Addgene 48138
pLKO5.sgRNA.EFS.PAC	(Heckl et al., 2014)	Addgene 57825
CRISPRv2 GFP	(Walter et al., 2017)	Addgene 82416
pSpCas9(BB)-2A-mCherry	In House	N/A
Software and Algorithms		
Trim Galore (v0.5.0)	Babraham Institute	RRID:SCR_011847
Picard (v 2.19.0)	Broad Institute	RRID:SCR_006525
RSEM	Dewey lab	RRID:SCR_013027
DESeq2 (v1.30.1)	Michael Love	RRID:SCR_015687
Cell Ranger (v6.0.1)	10X Genomics	RRID:SCR_017344
Slingshot (v1.8.0)	Kelly Street	RRID:SCR_017012
STAR (v 2.7.5a)	Alexander Dobin	RRID:SCR_004463
Seurat (v4.0.4)	Satija lab	RRID:SCR_016341
tradeSeq (v1.4.0)	Lieven Clement	RRID:SCR_019238
clusterProfiler (v3.18.1)	Guangchuang Yu	RRID:SCR_016884
R (v 4.0.5)	R project	RRID:SCR_001905
RUVseq (v1.24.0)	Davide Risso	RRID:SCR_006263
FlowJo v10	FlowJo, LLC	RRID:SCR_008520
Slidebook 6	Intelligent Imaging Innovations	RRID:SCR_014300
GraphPad Prism 9.0	GraphPad Software	RRID:SCR_002798
IMARIS 9.8	Oxford Instruments	RRID:SCR_007370